Prediction of recoater crash in laser powder bed fusion additive manufacturing using graph theory thermomechanical modeling

Abstract

The objective of this work is to predict a type of thermal-induced process failure called recoater crash that occurs frequently during laser powder bed fusion (LPBF) additive manufacturing. Rapid and accurate thermomechanical simulations are valuable for LPBF practitioners to identify and correct potential issues in the part design and processing conditions that may cause recoater crashes. In this work, to predict the likelihood of a recoater crash (recoater contact or impact) we develop and apply a computationally efficient thermomechanical modeling approach based on graph theory. The accuracy and computational efficiency of the approach is demonstrated by comparison with both non-proprietary finite element analysis (Abaqus), and a proprietary LPBF simulation software (Autodesk Netfabb). Based on both numerical (verification) and experimental (validation) studies, the proposed approach is found to be 5 to 6 times faster than the non-proprietary finite element modeling and has the same order of computational time as a commercial simulation software (Netfabb) without sacrificing prediction accuracy.

Keywords: Recoater Crash, Laser Powder Bed Fusion, Graph Theory, Thermomechanical Modeling.

1 Introduction

1.1 Objective and Motivation

The objective of this work is to predict a type of thermal-induced process failure called recoater crash (recoater impact or contact) that occurs frequently during laser powder bed fusion (LPBF) metal additive manufacturing. In LPBF thin layers of powder are deposited (raked or rolled) and selectively melted using energy from a laser to form a three-dimensional part [1]. A schematic of the LPBF process is shown in Figure 1.

The LPBF process can significantly improve functional performance of components used in strategic applications ranging from aerospace to biomedical industries [2, 3]. For instance, using LPBF to make an aircraft engine decreased the number of parts from 855 to 12, and increased fuel efficiency as well as engine power by 20% [4]. However, high process failure rates and inconsistent part quality currently afflict the throughput of LPBF [5-8]. Precision-oriented industries are therefore hesitant to use LPBF for making safety-critical parts [9-11]. Hence, to ensure broader use of LPBF parts, potential causes of flaw formation must be understood, predicted, and mitigated.

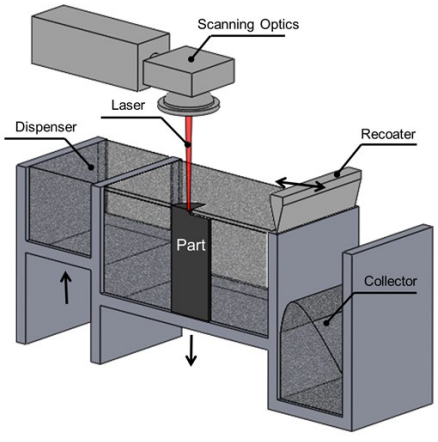

Figure 1: A schematic of the laser powder bed fusion (LPBF) additive manufacturing process.

Flaw formation in LPBF parts is chiefly influenced by the spatiotemporal temperature distribution – thermal history – as they are being printed [1]. It is estimated that thermal-induced deformations (distortion) are responsible for nearly 70% of LPBF build failures [12, 13]. To explain further, to make an LPBF part, a laser melts individual tracks of material at scanning speeds close to 1,000 $mm \cdot s^{-1}$. Consequently, the heating and cooling cycles often exceed 10^5 degrees $°C \cdot s^{-1}$ with meltpool temperature nearing the boiling point of the material [14-17]. The thermal history is a complex function of the part shape, material properties, and over 50 processing parameters [18-20]. Therefore, parameters optimized by empirical testing of simple-shaped coupons may not work when used for making complex parts [21].

Recoater crash is a type of frequently occurring build failure that is directly related to the thermal history [12, 13]. The aftermath of a recoater crash is shown in Figure 2 (top) which depicts an LPBF build plate consisting of Inconel 718 parts of different shapes. All these parts were built under identical processing conditions, which are detailed in Sec. 4.1. Near the left edge of the build plate are five arch-shaped parts; four of these five parts failed to build due to a recoater crash.

Uneven heating and cooling during the process causes the part to deform. Consequently, its top surface extends (raises) above the thin layer of powder. This phenomenon is called superelevation. In Figure 2 (bottom), superelevation is evident during printing of the arch and N-shaped parts [22]. If the superelevation (deformation) of the part in the vertical direction exceeds the clearance between the recoater and powder bed (typically between 20 to 50 μm), the part will interfere with the recoater as it attempts to deposit a new layer of powder. The resulting contact of the part with the recoater may damage the part; fine features are particularly vulnerable. A recoater crash may also damage the recoater itself requiring its replacement. Further, often following a

crash, the recoater drags debris from the failed part across the build plate, damaging other parts in the vicinity. It is common to discard an entire build due to a recoater crash.

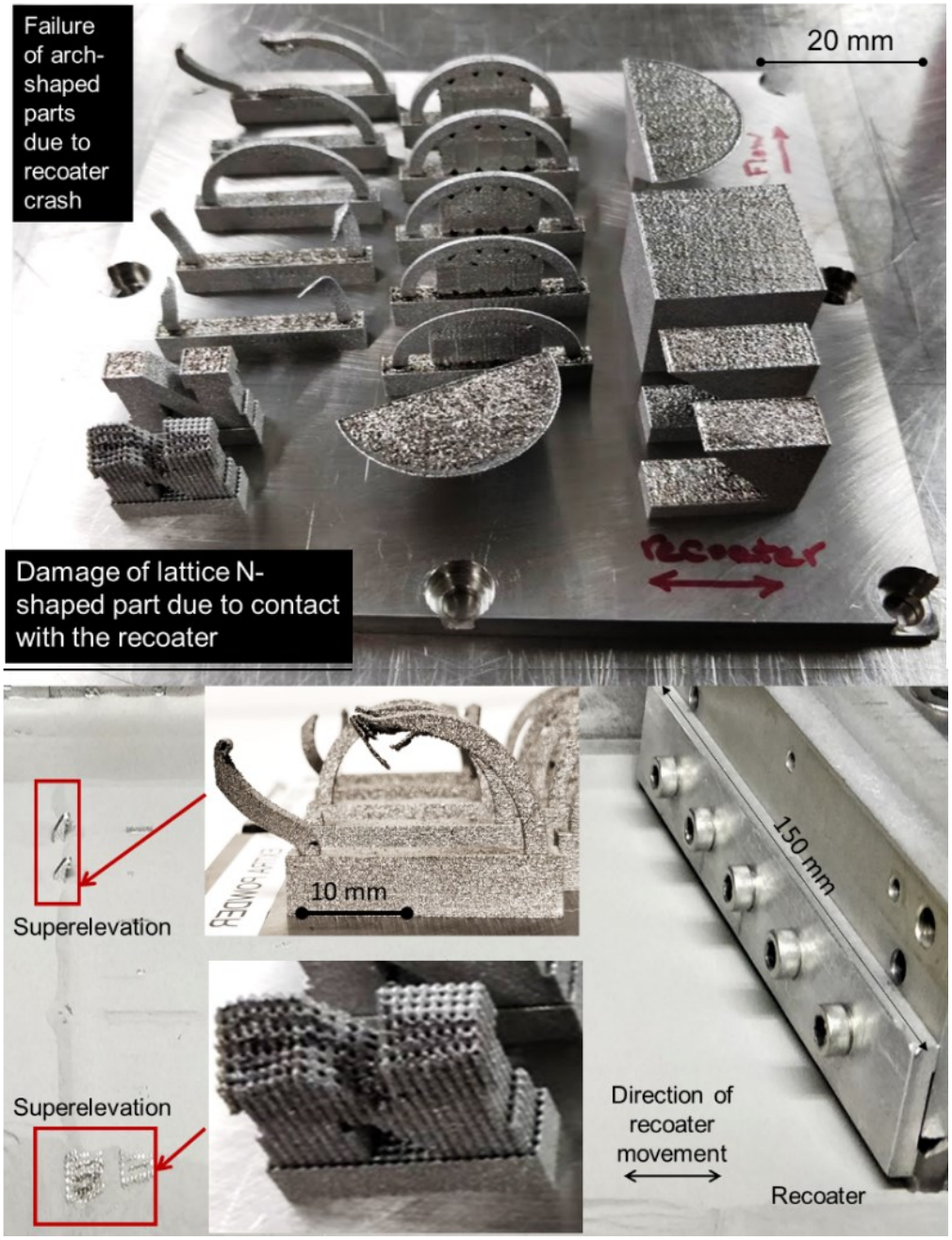

Figure 2: (Top) The build plate used for the experimental validation in this work, note the failed arch-shaped parts and damage to the lattice-like N-shaped part. (Bottom) The superelevation of the arches and N-shaped part leads to a subsequent recoater crash.

In Figure 2 (top), it is observed that the arch-shaped parts built with support structures did not fail, unlike their counterparts without supports. The arches without supports tend to retain heat, leading to the uneven temperature distribution. Supports, by providing a conduit for rapid conduction mitigate heat retention in the part, and thus curtail superelevation. The foregoing example from Figure 2 illustrates the consequential effect of part design on build quality in LPBF.

Thermal-induced failures, including recoater crashes, can be prevented through pragmatic design of the part geometry and optimization of processing conditions (placement and orientation of parameters, parameter selection, among others) [12, 23]. Currently, practitioners resort to an empirical build-and-test approach to avoid recoater crashes – an expensive and time-consuming process. Moreover, such empirical optimization efforts are only valid for a particular build plan because the addition or removal of parts from the build plate changes the thermal history [24]. In the context of Figure 2, fast and accurate thermal simulations that can replace trial-and-error experiments are critical for reducing build failures and facilitating production-level scaling of LPBF parts.

In this work recoater crashes are predicted using a graph theory-based computational thermomechanical modeling approach. We test this approach through verification (Sec. 3) and experimental validation (Sec. 4) studies following procedures recommended in the literature [25]. In the verification studies (Sec. 3), we compare predictions deformation and recoater crash predictions obtained from the graph theory-based model, with non-proprietary finite element-derived predictions (implemented in Abaqus with identical assumptions). Experimental validation is reported in the context of the arch-shaped objects (with and without supports) exemplified in Figure 2 (top). For the experimental validation, the graph theory predictions are compared with

both non-proprietary models and commercial LPBF modeling software (Netfabb). Netfabb is a non-linear FE-based thermo-mechanical simulation package.

We reiterate that the focus is to predict recoater crashes, which are caused by out of plane deformation of the part in the z-direction (vertical build direction). Accordingly, the deformation predictions reported in this work are restricted to those in the z-direction that occur during printing. However, apart from recoater crashes, deformation of the part during printing is also responsible for other types of build failures, such as shearing of anchoring supports during the process. Indeed, after printing the part may also crack or warp (deform) in three dimensions when it is separated from the build plate due to thermal-induced residual stresses. This work does not report results for failure of supports, nor does it predict warping when the part is removed from the build plate. In the forthcoming Sec. 1.2, we place this work in the context of the existing literature in thermomechanical modeling in LPBF.

1.2 Literature Review

The finite element (FE) method is a widely used approach for predicting thermal-induced deformation in LPBF. Gouge *et al.* [25-27], Luo *et al.* [28], DebRoy *et al.* [29], Bandyopadhyay *et al.* [14], Wei *et al.* [16], and Schoinochoritis *et al.* [30] have recently published comprehensive review articles on thermomechanical modeling in AM. Based on various computational strategies, the available thermomechanical models to predict thermal-induced deformation in AM are categorized as shown in Figure 3, and described herewith.

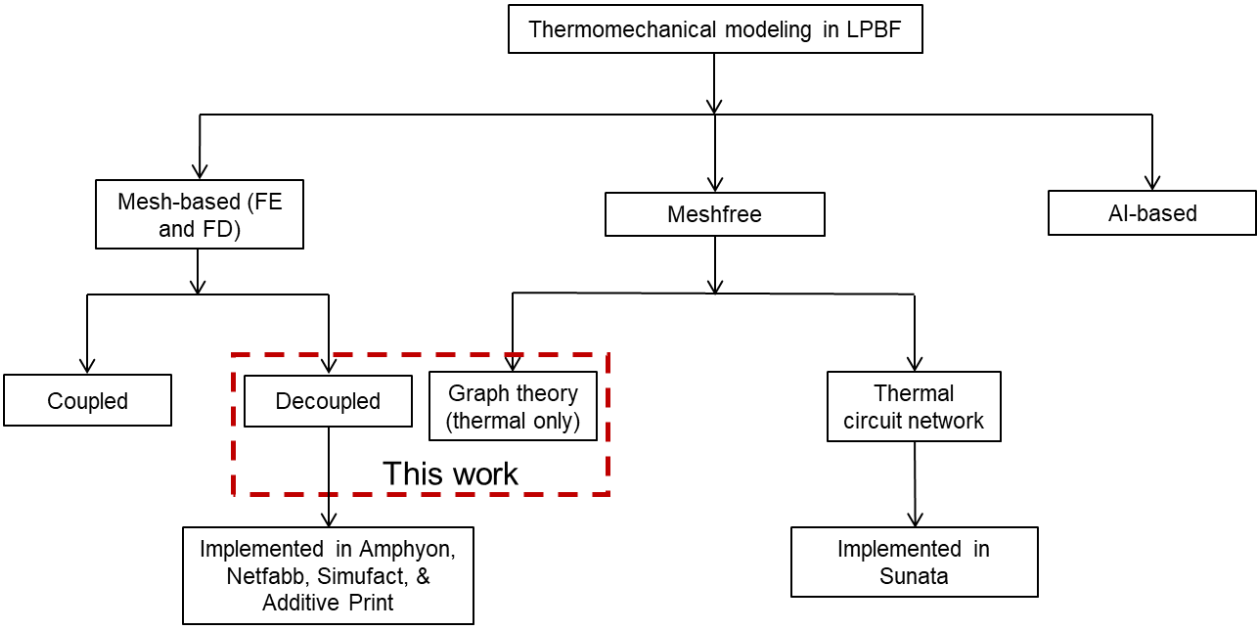

Figure 3: Modeling approaches to predict thermal-induced deformation categorized based on the computational technique.

(1) Coupled thermomechanical models

In coupled thermomechanical modeling the nonlinear thermal and mechanical equations are solved at every time step of the entire simulation. In other words, the thermal history and mechanical responses (residual stress, and deformation) are computed simultaneously [25, 31-37]. The coupled thermomechanical FE model can provide precise thermal and mechanical solutions compared to the decoupled thermomechanical model albeit at the cost of computational efficiency.

In this context, Ganeriwala *et al.* developed a coupled discrete finite-difference thermomechanical model [38].

(2) Decoupled thermomechanical model

In this commonly applied modeling approach, a thermal simulation of the LPBF part are conducted over several time steps, and then the thermal history predictions over this longer horizon is used to estimate the mechanical response [39-46]. The thermal and mechanical aspects are thus considered independent (decoupled); while the thermal history influences the mechanical response, the mechanical response is assumed to have no effect on the thermal response. Commercial LPBF simulation software such as Autodesk Netfabb, Amphyon, Simufact, and Additive Print implement this approach [47].

The benefit of decoupled thermomechanical modeling is that the computation is more efficient than coupled thermomechanical approach and provides reasonable prediction accuracy. However, the decoupled thermomechanical model loses fidelity when the distortion is sufficiently severe to change the boundary conditions. A change in boundary conditions can result from substantial change in the shape of the part, such as separation of anchoring supports, cracking and delamination which fundamentally changes the thermal conduction pathway.

This work also uses a decoupled thermomechanical modeling approach. It sequentially couples a meshfree, graph theory-based thermal model with a FE mechanical model. The graph theory modeling approach is discussed in detail in the forthcoming Sec. 2.

(3) Meshfree approaches

Apart from innovations in adaptive meshing and other computational simplifications to FE simulations, researchers have explored meshfree techniques to reduce the computational expense [34, 48]. For example, Peng *et al.* introduced a thermal circuit network (TCN) model to predict the

thermal history of a part. Then using the thermal history from the TCN model is coupled with FE to predict thermomechanical behavior such as thermal stress, residual stress and distortion [47, 49]. The commercial software Sunata uses the TCN model [47]. While these models require less computation time than FE methods due to their mesh-free nature, they remain to be explored further for complex shapes. The graph theory approach for thermal analysis is also a mesh-free method.

(4) AI-based approaches

Researchers have recently implemented an AI-based approach in AM to predict thermal history, residual stress, and thermal-induced distortion. For example, Chowdhury *et al.* [50] developed an artificial neural networ-based model to investigate thermal-induced deformation. They used the model prediction to compensate for the geometric dimensional inaccuracy which occurs due to thermal-induced deformation. Francis *et al.* [51] introduced a recurrent neural network-based deep learning approach to predict thermal-induced distortion from sensor data. While, this deep learning machine learning approach offers automated feature learning and facilitates highly accurate distortion prediction.

However, machine learning approaches require high-performance computing with large physical memory (>100 GB) to incorporate a large amount of testing data (big data) during the training of the model [51, 52]. To reduce data dependency, Zhu *et al.*[52] proposed a physics-informed neural network framework (scientific machine learning) that couples the fundamental thermal physics of LPBF with data-driven machine learning models to predict meltpool-level phenomena. The resulting neural network is not only compact, but also incorporates the physical aspects of the process, such as material properties, and mass and heat transfer behavior of the meltpool.

2 Approach

The approach consists of five steps shown in Figure 4. First, in Step 1 – Step 3 the temperature distribution in the part after the end of each layer is predicted using the graph theory thermal model. Our previous work demonstrated that the graph theory approach reduces computation time by a factor of 5 for obtaining the thermal history compared to non-proprietary FE analysis [53-57]. As an example, in Ref. [53] the graph theory approach was verified with exact analytical solutions, finite element and finite difference methods for a variety of two-, and three-dimensional benchmark heat transfer problems. In Ref. [57] the approach was validated in the context of a large Φ160 mm × 25 mm impeller part with in-situ temperature measurements. Considering these prior works, in this paper,

we eschew detailed explanation of the graph theory approach, and provide a brief background of the concept in Sec. 2.1.

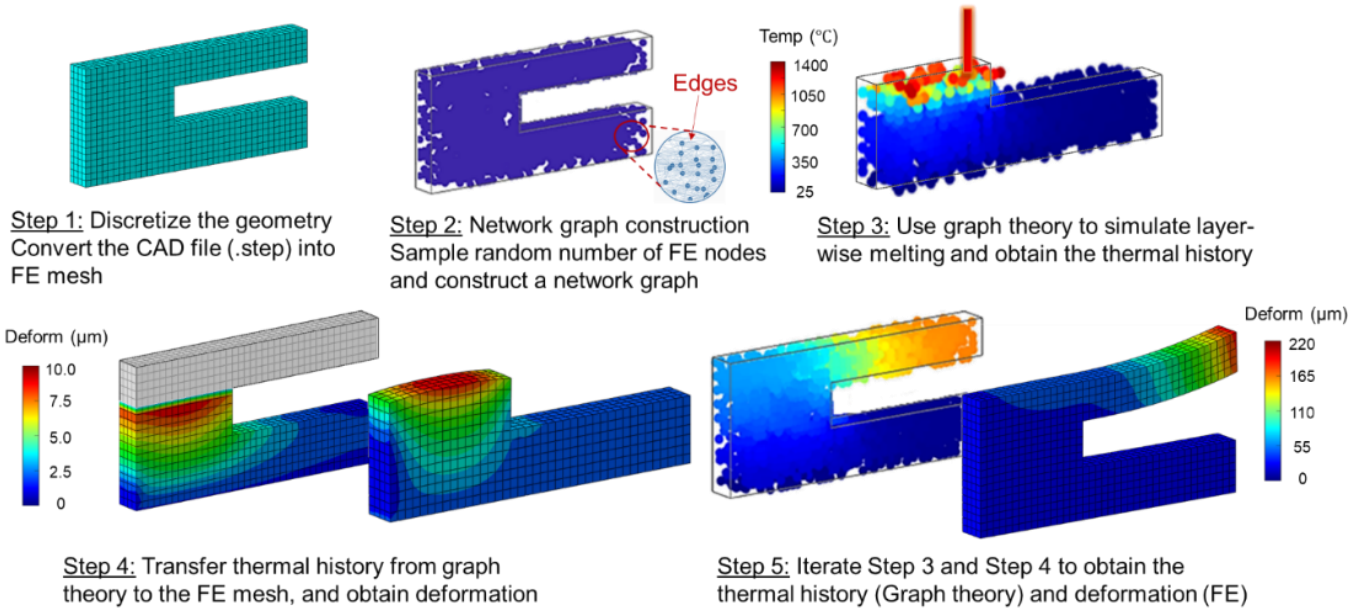

Figure 4: Schematic representation of graph theory approach in the context of the LPBF process.

In the second phase, Steps 4 and 5, the mechanical response, i.e., deformation in the z-direction) leading to recoater crash is predicted. For this purpose, the temperature distribution predictions obtained from graph theory at the end of a layer (Step 3) are exported to an uniform grid finite element mesh for predicting the distortion. The decoupled approach implemented in this work assumes that the thermal distribution influences the mechanical response, but the mechanical response does not influence the thermal history. The prediction of recoater crash is accomplished in Steps 4 and 5.

2.1 Background – Solving the Heat Diffusion Equation using Graph Theory

The thermal history of a part being printed in the LPBF process is predicted by solving the continuum heat diffusion equation [26].

$$\overbrace{\rho c_p}^{Material\ Properties}\frac{\partial \mathrm{T}(x,y,z,t)}{\partial t} - k\overbrace{\left(\frac{\partial^2}{\partial x^2}+\frac{\partial^2}{\partial y^2}+\frac{\partial^2}{\partial z^2}\right)}^{Laplacian}\mathrm{T}(x,y,z,t) = \overbrace{\mathrm{E}_V}^{Processing\ Parameters} \quad (1)$$

Here, the material density is ρ [kg·mm^{-3}], specific heat c_p [J·kg^{-1}·K^{-1}], thermal conductivity k [W·mm^{-1}·K^{-1}], T (x, y, z, *t*) is the instantaneous temperature at location (x, y, z) at time *t*. The second derivative term in the heat equation captures the effect of shape on the temperature distribution. This second derivative is called the *continuous Laplacian* [2]. On the right-hand side is the energy density $\mathrm{E_v}$ [W·mm^{-3}]; $\mathrm{E}_V = \frac{P}{\mathrm{v}\times\mathrm{h}\times\mathrm{t}\times\tau}$ is defined as the amount of energy supplied by the laser to melt a unit volume of powder. The volumetric energy density is a function of laser power (P) [W], scanning velocity (v) [m·s^{-1}], spacing between two consecutive laser tracks (h), [m], and layer thickness (t), [m], and time between layers (τ) [s].

To solve the heat diffusion equation boundary and initial conditions are added as follows:

$$\mathrm{T}(x,y,z,t=0) = \mathrm{T_p}\ \text{(Initially)} \quad (2)$$

$$k\frac{\partial \mathrm{T}}{\partial \mathrm{n}} + h\mathrm{T} = h\mathrm{T_P} = 0 \text{ (On boundary)}$$

In Eq.(2), h [W·mm^{-2}·K^{-1}] is the heat transfer coefficient, n is the outward normal vector at the boundary, and $\mathrm{T_P}$ [K] is the temperature of the surroundings. The boundary condition describes heat loss to the surroundings for $h \neq 0$; for $h = 0$ the boundaries are insulated (no heat loss).

The heat diffusion equation and the accompanying conditions are simplified by studying only one heating cycle at a time and by replacing the heat source term E_V with an initial temperature distribution. In Eqn. (3), below, the continuous Laplacian is represented as ∇^2 and the thermal diffusivity as $\alpha = \frac{k}{\rho c_p}$ [m^2·s^{-1}]

$$\begin{gathered}\frac{\partial \mathrm{T}(x,y,z,t)}{\partial t} - \alpha\nabla^2\mathrm{T}(x,y,z,t) = 0 \text{ (For one heating cycle)} \\ \mathrm{T}(x,y,z,t=0) = \mathrm{T_0}(x,y,z) = \mathrm{T_m}(x,y,z) \text{ (Initially)} \\ \frac{\partial \mathrm{T}(x,y,z,t)}{\partial n} = 0 \text{ (On boundary)}\end{gathered} \tag{3}$$

Shifting the heat source to the initial condition is reasonable for the LPBF where the laser scan is rapid compared to the long dwell time before the next layer is melted. The initial temperature distribution $\mathrm{T_0}(x,y,z)$ contains the peak temperature $\mathrm{T_m}$ which is the melting temperature of the material applied to the newly melted layer, and the initial temperature in the remainder of the body is the temperature distribution from the previous heating cycle. Another feature of this simplification is that the efficiency of transfer of laser energy into the material is not needed, as the energy delivered to the body is determined by the temperature of the newly melted layer.

Lastly, the above boundary condition has been changed to the insulated condition to accommodate the graph theory method. Heat loss at the boundaries is addressed separately, outside of the spectral graph method but within each deposition and heating cycle, as discussed later in Section 2.2. We note that the forgoing simplification is common to thermal modeling in LPBF [25, 26].

The graph theory approach approximates the continuous Laplacian with the Laplacian matrix L, in effect, $\nabla^2 = -\mathrm{L}$ [53]. The solution is obtained by discretizing the heat diffusion equation over N nodes and by replacing the continuous temperature with a discrete temperature vector (T),

$$\frac{\partial \mathrm{T}(x,y,z,t)}{\partial t} + \alpha \mathrm{L}\mathrm{T}(x,y,z,t) = 0 \tag{4}$$

The above is a first-order, ordinary linear differential equation, with solution [61],

$$\mathrm{T}(x,y,z,t) = e^{-\alpha L t}\mathrm{T_m}$$

The eigenvector matrix (ϕ) and eigenvalue matrix (Λ) of the Laplacian matrix (L) are found by solving the eigenvalue equation $\mathrm{L}\phi = \phi\Lambda$.

$$\mathrm{T}(x,y,z,t) = e^{-\alpha(\phi\Lambda\phi^{-1})t}\mathrm{T_m} \tag{5}$$

As the Laplacian matrix is symmetric and positive semi-definite, the eigenvalues (Λ) are non-negative, and the eigenvector matrix (ϕ) is orthogonal [58-61]. As the transpose of an orthogonal matrix is the same as its inverse, i.e., $\phi^{-1} = \phi'$.

Making the foregoing substitution in Eq. (5) gives,

$$\mathrm{T}(x,y,z,t) = e^{-\alpha(\boldsymbol{\phi\Lambda\phi'})t}\mathrm{T_m} \tag{6}$$

The term $e^{-\alpha(\phi\Lambda\phi')t}$ is simplified via a Taylor series expansion and substituting $\phi\,\phi' = \mathrm{I}$,

$$\begin{aligned} e^{-\alpha(\phi\Lambda\phi')t} &= \mathrm{I} - \frac{\phi\Lambda\alpha t\phi'}{1!} + \frac{(\phi\Lambda\alpha t\phi')^2}{2!} - \frac{(\phi\Lambda\alpha t\phi')^3}{3!} + \cdots \\ &= \mathrm{I} - \frac{\phi\Lambda\alpha t\phi'}{1!} + \frac{(\phi\Lambda\alpha t\phi')(\phi\Lambda\alpha t\phi')}{2!} - \frac{(\phi\Lambda\alpha t\phi')(\phi\Lambda\alpha t\phi')(\phi\Lambda\alpha t\phi')}{3!} + \cdots \\ &= \mathrm{I} - \frac{\phi\Lambda\alpha t\phi'}{1!} + \frac{\phi'(\Lambda\alpha t)^2\phi'}{2!} - \frac{\phi(\Lambda\alpha t)^3\phi'}{3!} + \cdots \end{aligned} \tag{7}$$

$$e^{-\alpha(\phi\Lambda\phi')t} = \phi e^{-\alpha(\Lambda)t}\phi'$$

Substituting, $e^{-\alpha(\phi\Lambda\phi')t} = \phi e^{-\alpha\Lambda t}\phi'$ into Eq. (6) gives,

$$\therefore \mathrm{T}(x,y,z,\Delta\mathrm{t}) = \phi e^{-\alpha g\Lambda\Delta\mathrm{t}}\phi'\mathrm{T_m}(x,y,z) = \phi e^{-\alpha g\Lambda\tau}\phi'\mathrm{T_m}(x,y,z) \tag{8}$$

Eqn. (8) is the graph theory solution to the discrete heat diffusion equation as a function of the eigenvalues (Λ) and eigenvectors (ϕ) of the discrete Laplacian Matrix (L), constructed on a discrete set of nodes [53]; and $\Delta t = \tau$ is the time between layers or inter-layer time. Notably, the solution is free of matrix inverse computations is semi-analytic, it is analytic in time and discrete (numeric) in space. To avoid truncation errors, the entire eigen spectrum consisting of n (number of nodes) eigenvectors (ϕ) and eigenvalues (Λ) are considered.

A parameter is introduced in Eqn. (9) to tune the units of the graph theory solution. We call this parameter a gain factor g (m^{-2}). The gain factor depends on material properties and node density which influences the diffusion rate of the graph theory solution. A thorough analysis of the effect of gain factor g is investigated in our previous work [55]. The term Δt is the time step. In this work, T_m is the melting point of Inconel 718, T_0 = ~1400 °C. To reduce the computational burden, we simulate the deposition and melting of several layers. This technique called the super layer or meta-layer approach is commonly used in LPBF as it reduces the simulation time, compared to a layer-by-layer approach while without drastically degrading computational accuracy [40, 62-64].

The graph theory approach for predicting the thermal history has three salient aspects that facilitate rapid computation of the thermal history: (1) it is mesh-free; (2) involves only matrix transpose and multiplication and not matrix inversion, and (3) does not require stepping through time in the simulation as the time step Δt can be set to any value.

The largest amount of computation in the graph theory approach is expended in the eigen decomposition of the Laplacian matrix (L) (over 70% of the total time). The computation cost to perform the eigen-decomposition of the Laplacian matrix is $O(rn^2)$, where r is the ratio of nonzero

elements, and n is the number of nodes [65]. However, L is symmetric, diagonally dominant with negative off-diagonal elements (M-matrix), and positive semi-definite. These properties facilitate rapid computation of the eigenvectors and eigenvalues in Matlab. The manner in which the graph theory approach is adapted for thermal modeling in LPBF, and subsequently combined with finite element modeling for mechanical analysis, is described in Steps 1 through 5. In closing this section, we have compared the graph theory solution with the exact analytical solution (Green's functions), finite difference (FD) and finite element (FE) methods for benchmark heat transfer problems in Ref. [53, 66].

2.2 Thermomechanical Analysis for Recoater Crash Prediction in LPBF

Step 1: Discretization of the geometry into nodes

The entire (desired) part geometry, in the form of a STEP file, is transformed into a FE mesh which also generates a set of discrete nodes. The position of these nodes is recorded in terms of their spatial coordinates (x, y, z).

Step 2: Network graph construction

A fixed number of N nodes are sampled randomly from the FE-generated nodes obtained from Step 1. In this work, the random sampling is adjusted such that a constant volumetric density of nodes (n nodes·mm^{-3}) is selected. These nodes are then used to obtain the thermal history using graph theory. The temperature history of the node located at (x, y, z) at a simulation time step Δt is T(x, y, z, Δt). The spatiotemporal temperature distribution obtained from graph theory simulation for the whole part is stored in a tensor **T**.

The N randomly sampled nodes, are binned into their respective layers and a network graph is constructed by connecting these nodes based on their spatial distance. The link connecting the

nodes is known as an edge. Nodes in layers where the material is deposited are termed active nodes, and those nodes that belong in layers that are yet to be deposited are termed inactive nodes.

Next, to avoid the non-physical effects of connecting nodes that are far away from each other only connect a fixed number of nearest nodes within the ε-neighborhood of a node. Consider an active node π_i at the center of a sphere of radius ϵ (mm). The active nodes that fall inside or on the surface of the sphere are called the neighbors of π_i. The radius of the sphere is termed as neighborhood distance (ϵ) and is a tunable parameter. The neighborhood distance defines the spatial discretization in the method and is roughly equivalent to the grid spacing in finite difference methods or the element size in finite element methods. The neighborhood distance is chosen based on the geometry of the part to be modeled. A guideline is to set the neighborhood distance no greater than the dimension of the finest feature in a part, called the characteristic length [55]. The characteristic length is defined as the distance that separates the neighboring geometries from being connected physically. The neighborhood distance should be smaller than the characteristic length. In effect, the neighborhood distance prevents nodes being connected across powder. In this work, we set ε = 2 mm for all parts studied.

To further reduce the computation burden we make the network graph sparse by removing edges. This is done by connecting the node π_i to its fifteen nearest nodes with an edge. These parameters are identical to our previous work [54, 56, 57]. Next, the Euclidean distance between two connected nodes (e.g., node π_i and a node π_j whose spatial Cartesian coordinates are $c_i(x_i, y_i, z_i)$ and $c_j(x_j, y_j, z_j)$, respectively) is computed, and weight $a_{i,j}$ is assigned to each edge based on the Gaussian function (also called the heat kernel),

$$d\left(c_i, c_j\right) = \left\|c_i - c_j\right\|^2 = (x_i - x_j)^2 + (y_i - y_j)^2 + (z_i - z_j)^2 .$$
$$a_{i,j} = e^{\frac{-d\left(c_i, c_j\right)}{\sigma^2}} \quad \forall\, i \neq j, d\left(c_i, c_j\right) \leq \varepsilon$$
$$a_{i,j} = 0, \text{otherwise} \tag{9}$$
$$\lim_{c_i - c_j \to 0} a_{i,j} = 1; \lim_{c_i - c_j \to \infty} a_{i,j} = 0$$

In other words, nodes beyond the neighborhood distance are not connected and no node is allowed to connect to itself. Further, the edge weight depends on the relative distance between the nodes and is between 0 and 1. The larger the edge weight between two nodes, the proportionally greater is the heat transfer between them. The quantity σ^2 in Eq. (9) is the variance obtained from the standard deviation of the Euclidean distance $d\left(c_i, c_j\right)$ between all node pairs.

Next, an adjacency or similarity matrix is formed by placing $a_{i,j}$ in row i and column j,

$$\mathrm{A} = [a_{i,j}].$$
$$\mathrm{A} = \begin{bmatrix} 0 & a_{1,2} & a_{1,3} & \cdots & a_{1,\mathrm{N}} \\ a_{2,1} & 0 & a_{2,3} & \cdots & a_{2,N} \\ a_{3,1} & a_{3,2} & 0 & \cdots & a_{3,N} \\ \vdots & \vdots & \vdots & \ddots & \vdots \\ a_{\mathrm{N},1} & a_{\mathrm{N},2} & a_{\mathrm{N},3} & \cdots & 0 \end{bmatrix} \tag{10}$$

The adjacency matrix is an N × N symmetric matrix, hence, $a_{i,j} = a_{j,i}$, where N represents the number of randomly sampled nodes. A degree matrix, D is formed by summing the rows of the adjacency matrix A and placing the sums in the i$^{\text{th}}$ diagonal. The diagonal entries $d_{i\cdot}$ are positive and off-diagonal entries are zero.

$$d_{i\cdot} = \sum_{j=1}^{N} a_{i,j}$$
$$\mathrm{D} = \begin{bmatrix} d_{1\cdot} & 0 & 0 \\ 0 & \ddots & 0 \\ 0 & 0 & d_{\mathrm{N}\cdot} \end{bmatrix} \tag{11}$$

The discrete graph Laplacian matrix is constructed as,

$$\mathrm{L} = \mathrm{D} - \mathrm{A}$$

$$\mathrm{L} = \begin{bmatrix} +d_{1\cdot} & -a_{1,2} & -a_{1,3} & \cdots & -a_{1,\mathrm{N}} \\ -a_{2,1} & +d_{2\cdot} & -a_{2,3} & \cdots & -a_{2,N} \\ -a_{3,1} & -a_{3,2} & +d_{3\cdot} & \cdots & -a_{3,N} \\ \vdots & \vdots & \vdots & \ddots & \vdots \\ -a_{\mathrm{N},1} & -a_{\mathrm{N},2} & -a_{\mathrm{N},3} & \cdots & +d_{\mathrm{N}\cdot} \end{bmatrix} \tag{12}$$

The Laplacian matrix falls under the category of a Stieltjes matrix as all its elements are real, it is symmetric and diagonally dominant with all off-diagonal elements non-positive. The Laplacian matrix is positive semi-definite. As a consequence of these properties of the Laplacian matrix, the eigenvalues (Λ) and eigenvectors (Φ) can be rapidly obtained by solving the eigenvalue problem $\mathrm{L}\Phi = \Phi\Lambda$ within Matlab.

Step 3: Simulate layer deposition and predict the temperature distribution

In this step, in every cycle, a new layer is deposited on the top of the previously deposited layers at its melting temperature (T_m). The heat on the top layer diffuses to the rest of the part via edges connecting the various nodes. The temperature at each node is determined at each time step $\Delta\mathrm{t}$ and stored in the temperature vector $\mathrm{T}(x, y, z, \Delta\mathrm{t})$.

The time between layers (TBL) is the time between the start of laser scanning of one layer to the start of scanning the next consecutive layer; it is the sum of the time it takes to scan a layer and recoat a fresh layer. For simulation, the TBL is divided into small timesteps $\Delta\mathrm{t}$.

The temperature at a node $\mathrm{T}(x, y, z, \Delta\mathrm{t})$ at time step $\Delta\mathrm{t}$ is a function of eigenvectors (ϕ) and eigenvalues (Λ) of the Laplacian matrix (L), determined by solving the first-order linear differential equation as discussed in the context of Sec 2.1.

$$\mathrm{T}(x,y,z,\Delta\mathrm{t}) = \phi e^{-\alpha g \Lambda \Delta \mathrm{t}} \phi' \mathrm{T}_0(x,y,z) = \phi e^{-\alpha g \Lambda \Delta \mathrm{t}} \phi' \mathrm{T}_m \quad (13)$$

Here initial temperature distribution $\mathrm{T}_0(x,y,z)$ contains newly melted material at, $\mathrm{T_m}$ which is the melting point of Inconel 718, about 1400 °C; and the remainder of the body is at the temperature from the end of the previous heating cycle. To reduce the computational burden, we simulate the deposition and melting of several layers. This technique called the super layer or meta-layer approach is commonly used in LPBF as it reduces the simulation time, compared to a layer-by-layer approach while without drastically degrading computational accuracy [40, 62-64].

To adjust the units to the solution of the heat equation, a parameter called gain factor g is introduced in Eq. (8). The effect of the gain factor g is discussed in depth in our previous work; it influences the diffusion rate [55]. The gain factor is contingent on the material type and node density. In this work, we set $g = 2 \times 10^6$ m^{-2}. This value is identical to those used in our previous work with Inconel 718 [56].

In Eq. (8) the temperature of a node $\mathrm{T}(x,y,z,\Delta\mathrm{t})$ is obtained by heat conduction within the body. As noted in Section 2.1, heat loss due to convection and radiation at the boundary is addressed within each heating cycle, but by a process outside of the graph theory method. Heat loss is included by applying lumped capacitive theory to the temperature at nodes on the boundary, as follows

$$\mathrm{T}_b = e^{-\tilde{h}\tau}\left(\mathrm{T}_{bi} - \mathrm{T}_p\right) + \mathrm{T}_p \quad (14)$$

Here, the temperature of the surroundings T_p is considered as constant, T_{bi} is the boundary node temperature obtained by the heat diffusion alone in Eq. (8), T_b is the resulting boundary node temperature incorporating convection and radiation heat loss, τ is the dimensionless time between layer depositions, and $\tilde{h}$ is the normalized cumulative coefficient of heat loss for convection (via

Newton's law of cooling) and radiation (via Stefan-Boltzmann law) from the boundary nodes to the surrounding powder and air. After convection and radiation are adjusted at boundary nodes, the temperature at various nodes obtained from graph theory at each node located at position (*x, y, z*) at time step Δt is $T(x, y, z, \Delta t)$. This spatiotemporal temperature distribution over time is stored as a tensor **T.**

Step 4: Predicting Distortion using FE

Step 4 is the bridge between the thermal history obtained using graph theory and the mechanical analysis from FE. The temperature (thermal history) at each node at the end of each layer stored in the tensor **T** from Step 3 is mapped (transferred) to its exact location on the FE mesh of the part generated in Step 1 for mechanical analysis. A linear interpolation function was used to map the thermal history spatially and temporally. Such an interpolation is often employed in the AM modeling literature though it introduces a small error in the model prediction [67]. Since the focus of this work is to predict recoater crashes, which occur when the deformation in the top layer of a part exceeds the clearance between the recoater and top of the powder bed (40 μm), we assume that elastic and thermal-induced strains dominate, and plastic strain is ignored. These assumptions is used frequently in the literature [68, 69].

The unidirectional relationship between the thermal and mechanical problems is an assumption that is widely applied in the LPBF field. Based on small deformation theory, as elucidated by Michaleris *et al.* [25, 26], this approach is valid when there are no major faults, such as cracking, the collapse of the supports, and separation of the part from the build plate. Such failures would not only alter the shape of the part but also change the heat conduction pathway, leading to considerable changes in the temperature profile.

In FE analysis, the thermal-induced deformation {U} is computed according to the following equations for elastic materials [47, 70]. The bottom face of the part is considered to be constrained (attached) to the substrate. A combination of displacement and traction boundary conditions is enforced to the entire part. The bottom face is in a fixed condition (i.e., $u = v = w = 0$) which means displacements in x, y, and z directions are zero. Where u, v, and w are the displacement components in x, y, and z directions. Traction boundary conditions $T^{(n)}$ is enforced at the specific nodes using thermal history. Moreover, the free surfaces (i.e., the surfaces between part and powder, and the top surface) are given traction free conditions, $T^{(n)} = 0$. The deformation of a node is obtained according to Eq. (15).

$$\{U\} = [K]^{-1}\{F_T\} \tag{15}$$

where {U} is the displacement vector; [K] the element stiffness matrix; and $\{F_T\}$ is the thermal load vector. These are obtained per Eq. (16) and Eq. (17),

$$[K] = \int [B]^T[H][B] \cdot dv \tag{16}$$

$$\{F_T\} = \int [B]^T[H]\, \alpha(\Delta \mathbf{T}) \cdot dv \tag{17}$$

Where the domain of integration is the volume of an element, [B] is the strain-displacement matrix, [H] is the elasticity matrix, α is the vector of thermal expansion coefficients, and $\Delta\mathbf{T}$ is the temperature difference between two nodes. For linear elastic isotropic materials, the elasticity matrix [H] is given by Eq. (18).

$$[\mathrm{H}] = \frac{\mathrm{E}}{(1+\nu)(1-2\nu)} \begin{bmatrix} 1-\nu & \nu & \nu & 0 & 0 & 0 \\ \nu & 1-\nu & \nu & 0 & 0 & 0 \\ \nu & \nu & 1-\nu & 0 & 0 & 0 \\ 0 & 0 & 0 & \frac{1-2\nu}{2} & 0 & 0 \\ 0 & 0 & 0 & 0 & \frac{1-2\nu}{2} & 0 \\ 0 & 0 & 0 & 0 & 0 & \frac{1-2\nu}{2} \end{bmatrix} \tag{18}$$

where E is the modulus of elasticity [$N \cdot m^{-2}$] and ν is the Poisson's ratio. The strain-displacement matrix [B] depends on the shape of the finite element used for analysis. In this study, we used eight-node hexahedral elements. The strain-displacement matrix for a hexahedral element is given by Eq. (19). This 8 node hexahedral mesh was chosen, as it is also used in the popular commercial LPBF simulation software, Netfabb.

$$[\mathrm{B}] = [\mathrm{B}_1 \quad \mathrm{B}_2 \quad \mathrm{B}_3 \quad \mathrm{B}_4 \quad \mathrm{B}_5 \quad \mathrm{B}_6 \quad \mathrm{B}_7 \quad \mathrm{B}_8]$$

$$[\mathrm{B_i}] = \begin{bmatrix} \frac{\partial N_i}{\partial x} & 0 & 0 \\ 0 & \frac{\partial N_i}{\partial y} & 0 \\ 0 & 0 & \frac{\partial N_i}{\partial z} \\ 0 & \frac{\partial N_i}{\partial z} & \frac{\partial N_i}{\partial y} \\ \frac{\partial N_i}{\partial z} & 0 & \frac{\partial N_i}{\partial x} \\ \frac{\partial N_i}{\partial y} & \frac{\partial N_i}{\partial x} & 0 \end{bmatrix} \tag{19}$$

where N_i is the shape function and is computed by Eq. (20).

$$\mathrm{N_i} = \frac{1}{8}(1 + \xi\xi_i)(1 + \eta\eta_i)(1 + \zeta\zeta_i) \tag{20}$$

where $\xi_i, \eta_i \; and \; \zeta_i$ denote the natural coordinates of node i; i = 1, 2, 3,…,8. In this analysis, it is assumed that the mechanical properties of the part are isotropic, and the elastic material behavior is considered only. Interpolation is used to scale temperature-dependent material properties between the build chamber temperature and the melting point.

Step 5: Obtain the thermal history and deformation for the entire part

Steps 3 and 4 are repeated until the entire part is finished, noting that the subsequent layers are simulated as being deposited on top of the previously deposited and deformed layer. Hence, the deformation of subsequent layers accounts for, and is in turn influenced by, dislocations in previous layers.

We reiterate that the proposed thermomechanical model is developed based on small deformation theory [25, 26]. The approach is valid when the LPBF part formation process is free of major flaws such as cracking, disintegration of the supports from the part or the build plate, and part separation from its original position on the build plate. Moreover, it ignores potential for deformation compensation due to the subsequent material deposition. As summarized in Sec. 1.2, this assumption is also common in FE-based commercial solutions, such as Netfabb.

3 Verification

3.1 Procedure

We applied the graph theory-based approach to predict deformation in the z-direction in two LPBF test parts (Figure 5). The verification procedure pertains to comparing both the thermal history and mechanical deformation predictions obtained from the decoupled solution from the proposed graph theory-based approach, termed graph theory (deformation), with a coupled thermomechanical FE model implemented in Abaqus. The coupled thermomechanical FE-based simulation serves as the ground truth to calibrate as well as evaluate the graph theory results. The comparison of the graph theory solution and the coupled thermomechanical FE solution is made in terms of the root mean squared error (RMSE) and mean absolute percentage error (MAPE) of the deformation predictions.

The coupled thermomechanical FE model was obtained using the DFLUX routine in Abaqus per the procedure widely used in the LPBF literature [71, 72]. The mechanical analysis phase (Step 4) of the graph theory approach is identical to the corresponding coupled thermomechanical FE-based analysis. Identical assumptions were imposed in both the coupled thermomechanical FE-based model and graph theory model, including the use of super-layers or meta-layers to ease the computational burden.

Both models also maintain identical mechanical boundary conditions and hexahedral mesh elements. The mechanical analysis part of the graph theory model uses the mesh element C3D8R in Abaqus (8-node linear brick, reduced integration, hourglass control). The coupled thermomechanical FE analysis uses the similar C3D8T mesh element (8-node thermally coupled brick, trilinear displacement, and temperature). We note that both element types are identical in shape, except that C3D8R does not facilitate thermal analysis.

3.2 Test Parts

To verify the graph theory-based solution with the coupled thermomechanical FE model two test parts were considered as shown in Figure 5. These are termed the C-shaped part without supports, Figure 5(a); and C-shaped part with supports, Figure 5(b). The C-shaped part without supports in Figure 5(a) has a large overhang feature, whose underside is not supported. The overhang region tends to accumulate heat leading to thermal-induced deformation, often leading to a recoater crash.

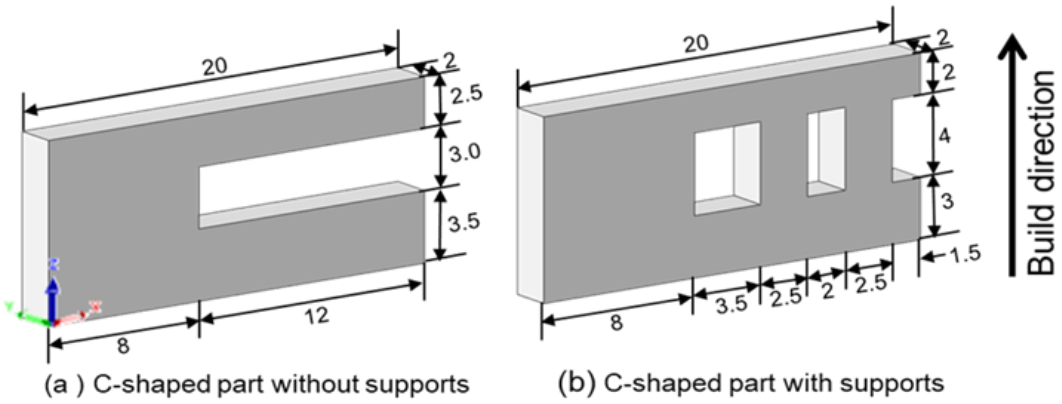

Figure 5: (a) C-shaped part without supports, (b) C-shaped part with supports.

The practical context for using the C-shaped parts as exemplar objects is further illustrated in Figure 6, which shows an LPBF knee implant. To prevent excessive heat accumulation at the overhang region and subsequent distortion, supports were built under the overhanging feature. Supports also anchor the part to the substrate so to avoid dislocation due to the lateral force of the recoater. To prevent the part from collapsing under its own weight, supports were built under the overhanging feature. However, these supports were too thin to prevent heat retention in the overhang region. Hence, after the build, the overhang area manifested overheating, resulting in coarse-grained microstructure and poor surface finish, which made the implant potentially unsafe for clinical use.

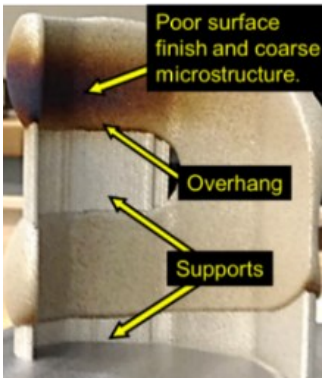

Figure 6: LPBF knee implant with thin supports showing overheating at the overhang region [57].

3.3 Model Calibration and Convergence Studies

The simulation parameters, material properties are shown in Table 1. The powder properties used in this analysis are of Inconel 718. The model calibration was performed based on the C-shaped part without supports and followed the recommendations of Gouge *et al.* [25, 26]. First, the thermal history predictions (thermal solution) obtained from graph theory were verified with its corresponding thermal solution obtained from the coupled thermomechanical FE simulation. Next, the thermal solution from graph theory was used as an input to the decoupled mechanical FE model to predict layer-by-layer deformation. The graph theory (deformation) solution was subsequently verified with the coupled thermomechanical FE-based simulation. In effect, the coupled thermomechanical FE model served as the ground truth.

Two parameters need to be calibrated in the approach. With super layer thickness fixed at 0.5 mm based on prior work, the first parameter is the number of nodes per unit volume in graph theory (node density, nodes·mm^{-3}) for thermal analysis in Step 1 – Step 3 [56]. The second parameter is the FE mesh element size for the prediction of deformation in Step 4. We note that an extensive convergence study for the coupled thermomechanical FE model was conducted to ascertain the element size. Five element sizes were studied, ranging from 2 mm × 2 mm × 2 mm to 0.3 mm × 0.3 mm × 0.3 mm, as summarized in Table 2.

Table 1: Summary of material properties and simulation parameters for graph theory and the coupled thermomechanical FE models [56, 73, 74].

Material properties and simulation parameters	Values
Material	Inconel 718
Density, ρ [kg·m^{-3}]	8,230
Thermal conductivity, k [W ·m^{-1} ·K^{-1}]	11.1
Specific heat, C_p [J ·kg^{-1} ·K^{-1}]	435
Thermal diffusivity (α) [m^{2}s^{-1}]	3.2×10^{-6}
Expansion coefficient [°C^{-1}]	12.1×10^{-6}
Young's modulus [N·m^{-2}]	2×10^{11}
Poisson's ratio	0.3
Melting Point, T_m [°C]	1,400
Build chamber temperature, T_{amb} [°C]	110
Convection coefficient wall to powder, h_w [W·m^{-2}· C^{-1}]	25 (C-shaped parts) 15 (arches)
Convection coefficient substrate (sink), h_s [W·m^{-2}· C^{-1}]	5000 (C-shaped parts), 2500 (arches)
Layer thickness [mm]	0.040
Super layer thickness [mm]	0.5
Gain factor, g [m^{-2}]	2×10^6
Time between layers, TBL [sec]	10 sec for both C-shaped parts, varies for arches based on experiment, see Ref. [56]
Computational hardware	Intel(R) Core (TM) i5-7500 CPU @ 3.40GHz with 16 GB RAM

Figure 7 shows the thermal history and maximum deformation in the z-direction (build direction) as a function of the layer height at a specific location (x = 4 mm, y = 1 mm, z mm) on the C-shaped part without supports; the origin is on the left front vertex of the part. The result obtained using the graph theory (red line) is overlaid on the temperature and deformation predictions from the coupled thermomechanical FE simulation (ground truth, black line), in Figure 7(a) and Figure 7(b), respectively. The results in Figure 7(a) show that the surface temperature predictions obtained from the graph theory thermal model converge to the coupled thermomechanical FE solution with the increase of the node density. Increasing the node density is advantageous to prediction accuracy as shown in recent work at the expense of the computation time [55].

The thermal history predictions at the end of each layer obtained from graph theory were imported into an FE model to obtain the mechanical solution. With the decrease in element size, model accuracy improves as is evident in Figure 7(b). As there is a tradeoff between the element size and the computation time, an element size of 0.5 mm × 0.5 mm × 0.5 mm was considered in this work based on convergence studies. The top surface temperature at a specific spatial location after completion of a layer was predicted using the graph theory approach. The solution was calibrated with respect to the temperature predicted by the coupled thermomechanical FE model as a function of the node density (nodes·mm^{-3}) with mesh size was set at 0.5 mm × 0.5 mm × 0.5 mm. Based on the calibration, we selected the node density as 5.0 (nodes.mm^{-3}) that yields MAPE ~1% and RMSE ~7 °C with respect to the coupled thermomechanical FE model.

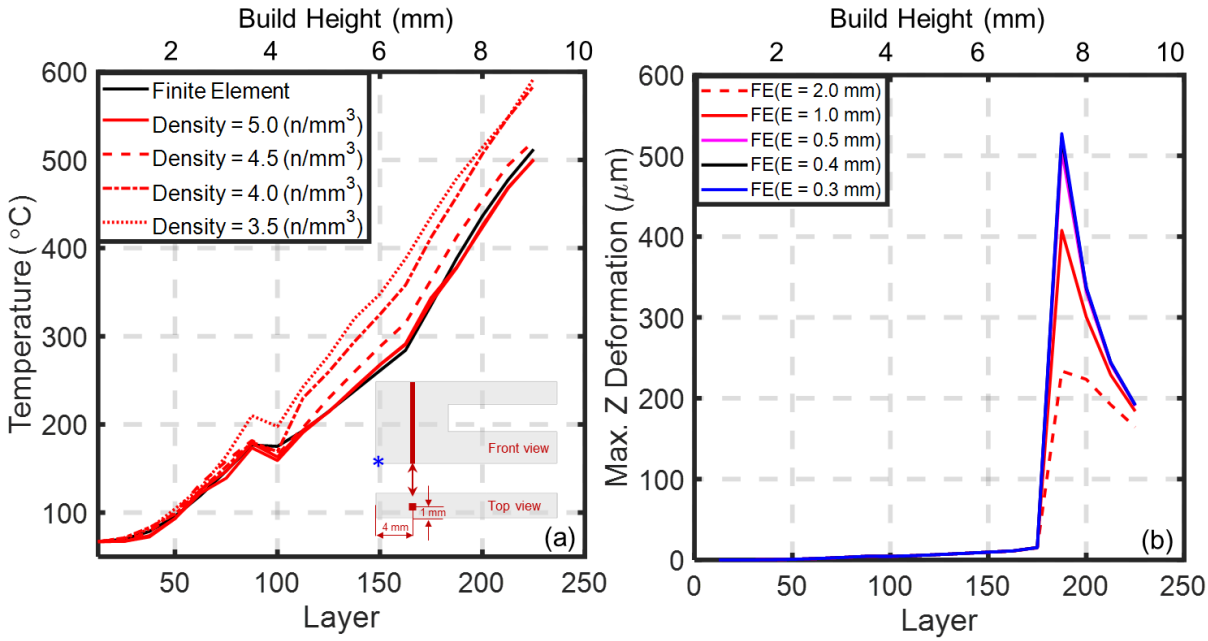

Figure 7: Calibration of (a) graph theory thermal model for node density as the number of nodes per mm^3 and (b) coupled thermomechanical FE model for mesh element size in mm. The asterisk* represents the origin (x = 0, y = 0, z = 0) of the C-shaped parts.

Table 2: Effect of the number of nodes on graph theory thermal prediction and element size on deformation prediction using FE.

Variables	Number of nodes	MAPE (%)	RMSE (°C)	Computation time (s)
Thermal history	1540 (selected)	1	7	11
	1295	3	17	10
	1230	6	48	9
	1080	9	62	8
Deformation	Element size (mm)	MAPE (%)	RMSE (μm)	Computation time (s)
	2 × 2 × 2	8	76	6
	1 × 1 × 1	3	30	16
	0.5 × 0.5× 0.5 (selected)	1	5	57
	0.4 × 0.4 × 0.4	0.15	1	92
	0.3 × 0.3 × 0.3	0	0	756

3.4 C-shaped Part without Supports

The part geometry as shown in Figure 5(a) was converted into a FE mesh. The mesh consisted of 2,624 elements (3705 nodes) having an approximate element size of 0.5 mm × 0.5 mm × 0.5 mm. These nodes were extracted from the FE model and employed in the graph theory model for predicting deformation, as described in Steps 2 through 5 in described in Sec. 3.1 (Figure 4).

3.4.1 Thermal History Prediction

The temperature predictions from the graph theory approach were obtained with node density set at 5 nodes·mm^{-3}. Shown in Figure 8(a) is the average surface temperature prediction at the end of the layer. Likewise, reported in Figure 8(b) and Figure 8(c) are the surface temperature at two specific locations, namely, (x = 4 mm, y = 1 mm, z mm) and (x = 7 mm, y = 1 mm, z mm), respectively. The temperature predictions using the graph theory (red line) are overlaid on the temperature predictions from the coupled thermomechanical FE simulation (ground truth, black line).

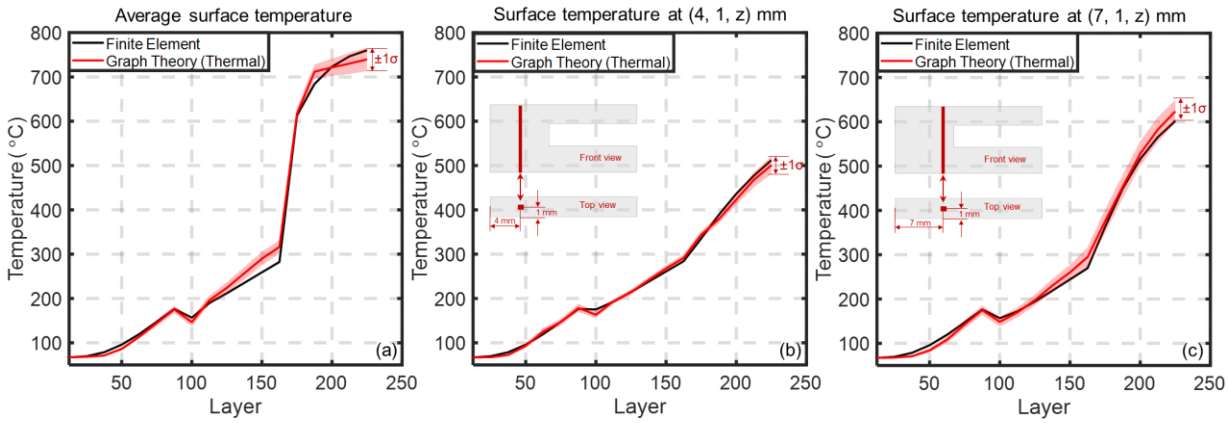

Figure 8: Thermal history of the C-shaped part without supports. (a) Average surface temperature measured at the end of the layer. (b) & (c) Surface temperature at a specific location (4, 1, z) mm and (7, 1, z) mm, respectively. The red line in the figure represents the thermal history predicted using the graph theory approach with ± 1 standard deviation over 10 replications, whereas the black line is the thermal history predicted using the coupled thermomechanical FE model which is considered as the ground truth.

The error in the graph theory thermal prediction with respect to the coupled thermomechanical FE model for the average surface temperature in Figure 8(a) is ~ 2% (MAPE) and ~16 °C (RMSE). Similarly, for the chosen location (x = 4 mm, y = 1 mm, z mm) reported in Figure 8(b) the MAPE and RMSE are ~ 1% and ~ 7 °C, respectively. At location (x = 7 mm, y = 1 mm, z mm) reported in Figure 8(c) the MAPE and RMSE are ~ 2% and ~ 12 °C, respectively.

The graph theory thermal prediction is bounded with ± 1 standard deviation over ten replications. The graph theory thermal simulation converged in ~ 6 seconds while the coupled thermomechanical FE reached the solution in ~ 58 seconds. The temperature distribution of the complete part obtained from the coupled thermomechanical FE, graph theory (Thermal), and Netfabb simulations is shown in Figure 9.

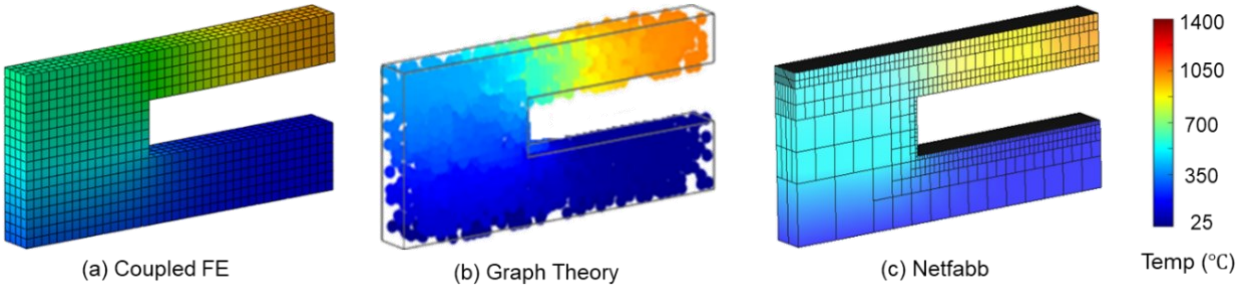

Figure 9: Qualitative comparison of thermal history predictions at the completion of the part from (a) coupled thermomechanical FE model, (b) graph theory (Thermal) model, and (c) Netfabb.

3.4.2 Deformation Prediction

The maximum top surface deformation predicted using graph theory is shown in Figure 10(a), and closely tracks the deformation obtained from the coupled thermomechanical FE simulation. The results are summarized in Table 3 and Table 4. The average deformation in each layer is shown in Figure 10(b). Next, shown in Figure 10(c) and Figure 10(d) are the deformations as a function of layer height at the specific locations (4 mm, 1 mm, z mm) and (7 mm, 1 mm, z mm), respectively. Layers 188 to 225 undergo considerable deformation due to heat accumulation in the overhang region.

From Figure 10(a) and Figure 10(b), we note that the deformation in the z-direction exceeds the layer thickness (40 µm) at a build height of 7 mm, indicating the possibility of a recoater crash. In these studies, the typical error in the graph theory approach in predicting deformation with respect to the coupled thermomechanical FE model is ~ 4-6% (MAPE) and ~ 0-9 µm (RMSE).

The deformation results for the C-shaped part in Figure 10, Table 3 and Table 4 are restricted to graph theory and FE model; results from Netfabb were not included due to the following reason. The C-shaped part was simulated (no actual part was built) with a constant time between layers (TBL) of 10 seconds (Table 1). In practice, the time between layers is not constant, but varies proportionally to the X-Y scanned area of the part. The Netfabb software determines the TBL for

every layer; based on the part geometry, processing parameters, and machine type; it does not provide the freedom to set a constant TBL. Hence, the quantitative comparison of deformation between the proposed model and the Netfabb is not feasible for the model verification with C-shaped part without supports, and C-shaped part with supports reported in the forthcoming section (Sec. 3.5). This limitation is precluded for model validation (Sec. 4), where actual parts were built. The TBL used in the graph theory model matches the experiment, and hence a quantitative comparison of deformation from FE, graph theory, and Netfabb is viable.

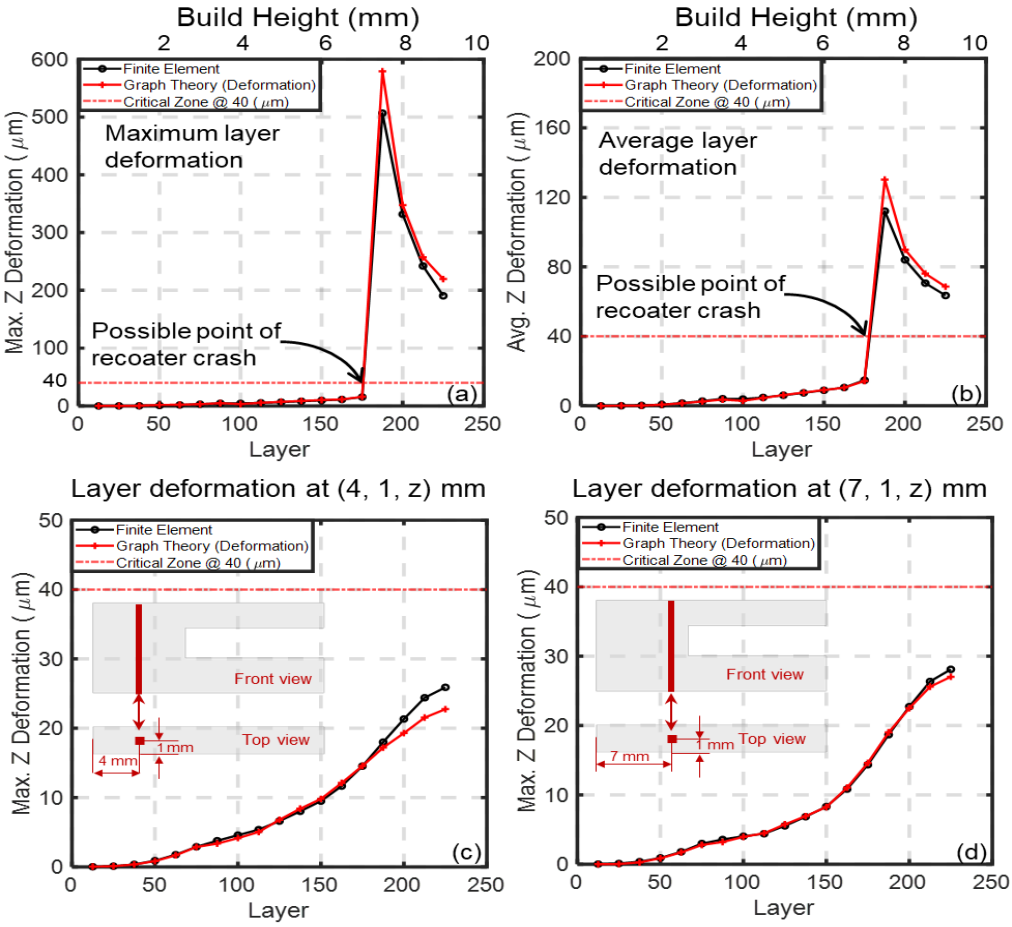

Figure 10: Comparison of predicted deformation of C-shaped part without supports between the coupled thermomechanical FE model and the graph theory-based approach showing (a) maximum deformation of each layer, (b) average layer deformation, and (c) & (d) deformation measured at (4, 1, z) mm, and (7, 1, z) mm, respectively, along the build direction.

Table 3: Graph theory (Deformation) model performance for C-shaped part without supports in terms of MAPE, RMSE, and computation with respect to coupled thermomechanical FE model. The MAPE and RMSE are estimated based on the maximum deformation of each layer.

Variables	Coupled thermomechanical FE Model	Graph theory (Deformation) model			
Node density (nodes/mm^3)	11.30	5.0	4.5	4.0	3.5
Node count	3705	1540	1295	1230	1080
MAPE (%)	Ground truth	6.30	11.11	13.31	14.89
RMSE (μm)	Ground truth	8.81	20.79	25.29	25.05
Computation time (s)	57.10	10.93	9.77	9.04	7.95

Table 4: Graph theory model performance for the estimation of deformation in terms of MAPE, RMSE, and computation with respect to coupled thermomechanical FE analysis for C-shaped part without supports.

Description	MAPE (%)	RMSE (μm)	Computation time (s)	
			Thermo-mechanical coupled FE model	Graph theory
Maximum layer deformation (Figure 10(a))	6.30	8.81	57.10	10.93
Average layer deformation (Figure 10(b))	6.09	4.83		
Deformation at (4, 1, z) mm (Figure 10(c))	5.90	1.26		
Deformation at (7, 1, z) mm (Figure 10(d))	3.94	0.48		

3.5 C-shaped Part with Supports

The C-shaped part with supports, Figure 5(b), was simulated using identical boundary conditions, material properties, and the simulation parameters of the C-shaped part without supports. Similar to the C-shaped part without supports, the geometry was converted into FE mesh. The mesh consisted of 2,752 elements (3885 nodes) having a size of 0.5 mm × 0.5 mm × 0.5 mm.

3.5.1 Thermal History Prediction

The coupled thermomechanical FE and graph theory thermal history predictions of the average surface temperature are overlaid in Figure 11 (a). The thermal predictions at two specific locations, namely, (4 mm, 1 mm, z mm), and (17 mm, 1 mm, z mm) are also overlaid in Figure 11(b) and Figure 11(c), respectively. The error in the thermal history of the graph theory approach in comparison to the coupled thermomechanical FE solution for average surface temperature is MAPE 2% and RMSE 23°C. At location (4 mm, 1 mm, z mm) the error in comparison to the coupled thermomechanical FE model is 1% (MAPE) and 10 °C (RMSE). At the second location (17 mm, 1 mm, z mm), the error is 3% (MAPE) and 28 °C (RMSE). The graph theory thermal simulation converged in ~7 seconds while the coupled thermomechanical FE simulation in ~61 seconds.

Shown in Figure 12 is a qualitative comparison of temperature distribution on the completion of the C-shaped part with supports obtained from the coupled thermomechanical FE model, graph theory thermal model, and Netfabb. Comparing Figure 11(a) and Figure 8(a) we note that the C-shaped part with supports depicts a more gradual decrease in surface temperature in contrast to the C-shaped part without supports. Further, the temperature of the final layer of the C-shaped part with supports is almost 200 °C lower than its counterpart without supports.

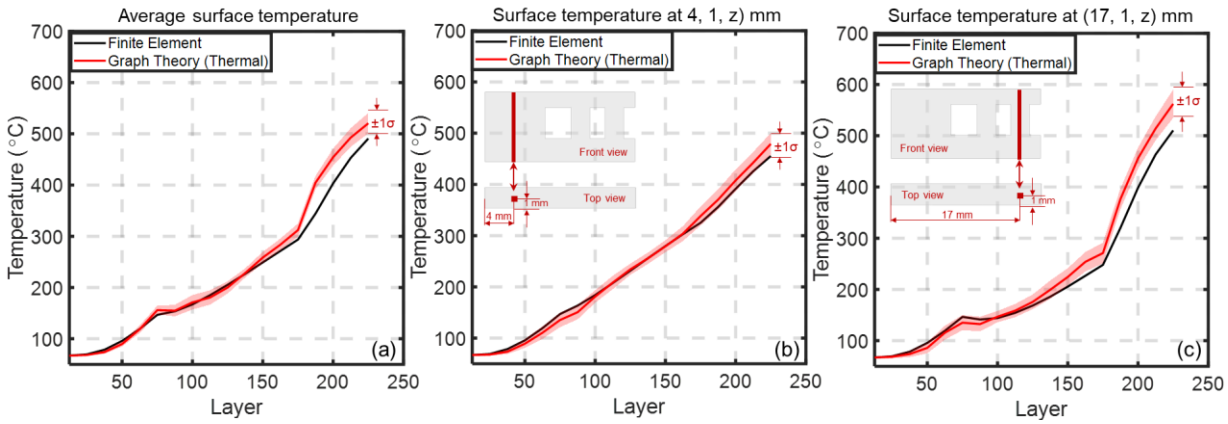

Figure 11: Thermal history of the C-shaped part with supports showing (a) average surface temperature at the end of each layer; (b) & (c) are the temperatures measured at two different coordinates for different layer heights of z (4 mm, 1 mm, z mm), and (17 mm, 1 mm, z mm), respectively.

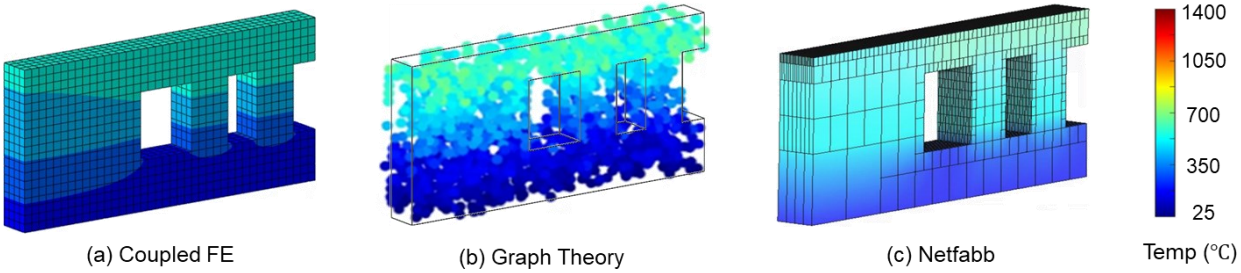

Figure 12: Qualitative comparison of the thermal history predictions at the completion of the part from (a) coupled thermomechanical FE model, (b) graph theory (Thermal) model, and (c) Netfabb.

3.5.2 Deformation Prediction

The deformation of the C-shaped part with supports was predicted using the coupled thermomechanical FE model and the graph theory (Deformation) approach at different locations. The results are depicted in Figure 13 and summarized in Table 5 and Table 6.

For the scenarios tested, the graph theory approach predicted the deformation in the z-direction with MAPE ~ 9% and 4 µm RMSE. The computation time of the graph theory approach was ~ 12 seconds compared to ~ 61 seconds with the coupled thermomechanical FE model. The benefits of using supports are evident in comparing Figure 13(a) and Figure 13(b), for the C-shaped part with supports alongside Figure 10(a) and Figure 10(b), respectively. The maximum and average layer deformation in the C-shaped part with supports is significantly less than 40 µm.

In other words, the C-shaped part with supports mitigates the tendency for a recoater crash by avoiding heat retention in the overhang region. The supports act as conduits to conduct the heat away from the overhang region. The prediction error (i.e., the MAPE and the RMSE) decreases with the increase of the node density (node per mm^3) as evident in Table 5.

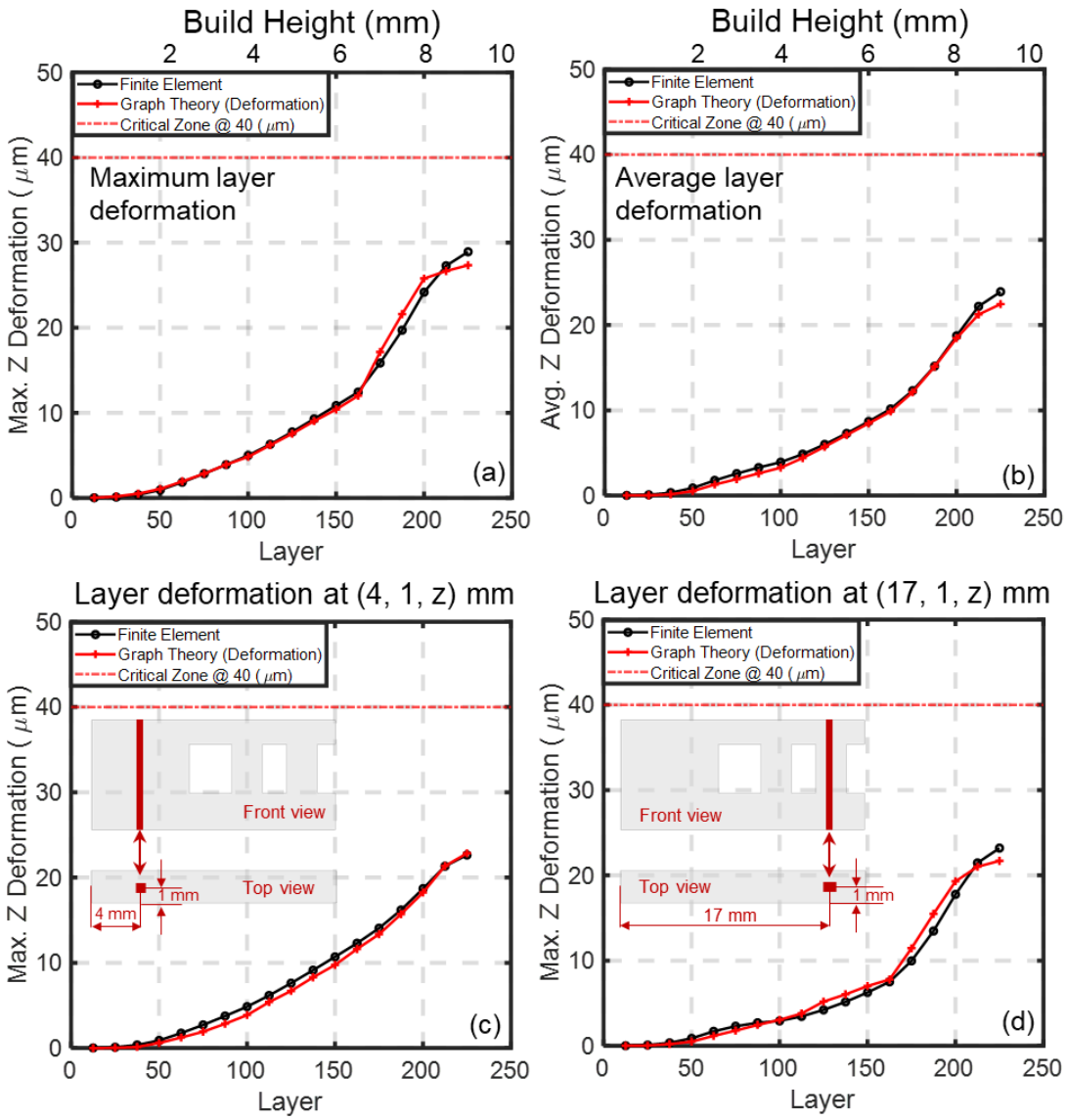

Figure 13: Comparison of deformation predictions for C-shaped part with supports between the coupled thermomechanical FE and the graph theory (Deformation) approaches.

Table 5: Graph theory (Deformation) model performance for the C-shaped part with supports in terms of MAPE, RMSE, and computation time with respect to the coupled thermomechanical FE model. The MAPE and RMSE are estimated based on the maximum deformation of each layer.

Variables	Coupled thermomechanical FE Model	Graph theory (Deformation) model			
Node density (nodes/mm^3)	11.30	5.0	4.5	4.0	3.5
Node count	3885	1620	1460	1295	1140
MAPE (%)	Ground truth	3.74	8.04	13.78	17.02
RMSE (μm)	Ground truth	1.28	2.07	2.58	3.67
Computation time (s)	60.70	11.56	11.10	9.83	8.59

Table 6: Graph theory model performance for the estimation of deformation in terms of MAPE, RMSE, and computation with respect to coupled thermomechanical FE analysis for C-shaped part with supports.

Description	MAPE (%)	RMSE (μm)	Computation time (s)	
			Thermo-mechanical coupled FE model	Graph theory
Maximum layer deformation (Figure 13(a))	3.74	1.28	60.70	11.56
Average layer deformation (Figure 13(b))	3.02	3.47		
Deformation at (4, 1, z) mm (Figure 13(c))	8.77	0.68		
Deformation at (17, 1, z) mm (Figure 13(d))	8.76	1.25		

4 Validation

4.1 Experiments

To validate the graph theory (deformation) approach for predicting recoater crashes, experiments were conducted on an open architecture LPBF platform at Edison Welding Institute, Ohio. These are detailed in Ref. [56]. The schematic and pictures of the setup are shown in Figure 14. The material was Inconel 718. The build required about 10 hours to complete. The system was integrated with a thermal camera inside the chamber to acquire the surface temperature measurements of the part as it was being built. The thermal camera was inclined at 80° to the horizontal. The thermal camera (Micro Epsilon, model TIM 640) had a spectral range of 8 to 14 μm (longwave infrared spectrum), and an optical resolution of 640 pixels × 480 pixels. The spatial resolution was ~20 pixels per mm^2.

The thermal camera was triggered to capture images of the powder bed only when the laser was actively melting a layer. The thermal camera stopped recording when the laser finished scanning a layer. In other words, the camera was turned on only when the laser was active. The thermal camera was calibrated to an absolute temperature scale using a reference thermocouple measurement [56].

The graph theory approach is applied to predict recoater crashes of the arch-shaped parts shown in Figure 15. There are two types of arch-shaped parts, namely, arches built with supports and those without supports. These parts are analogous to the C-shaped parts with and without supports studied in Sec. 3. As shown in Figure 15, all the arches have the same length of 40 mm and height of 26 mm, and base width of 5 mm but have varying gauge thicknesses (t) from 0.5 mm to 2.5 mm in steps of 0.5 mm. As first discussed in the context of Figure 2, all the arches without

supports, except the arch with gauge thickness t = 1.5 mm, failed during printing due to recoater crash.

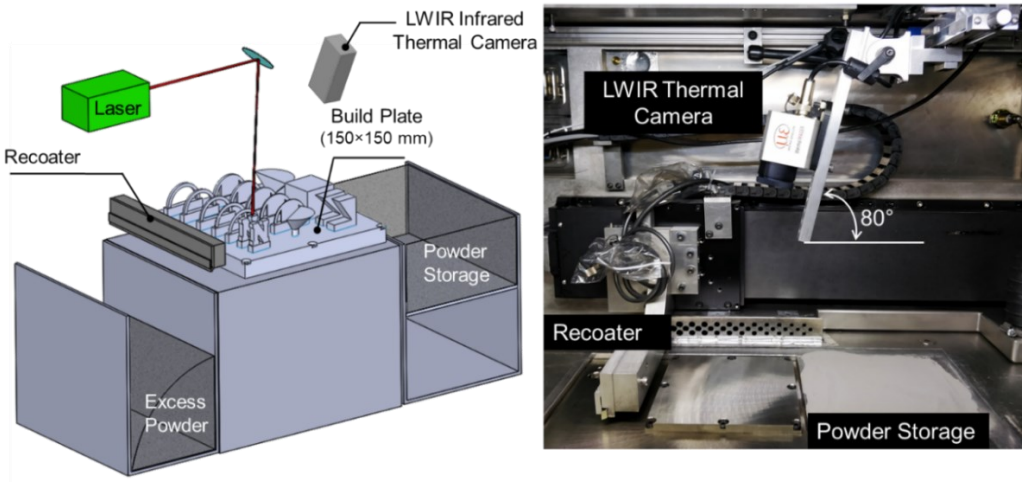

Figure 14: The schematic of the and photograph of the LPBF setup. A longwave infrared thermal camera located above the build plate and inclined at 80° to the horizontal plane is used to capture the part surface temperature during the build process [56].

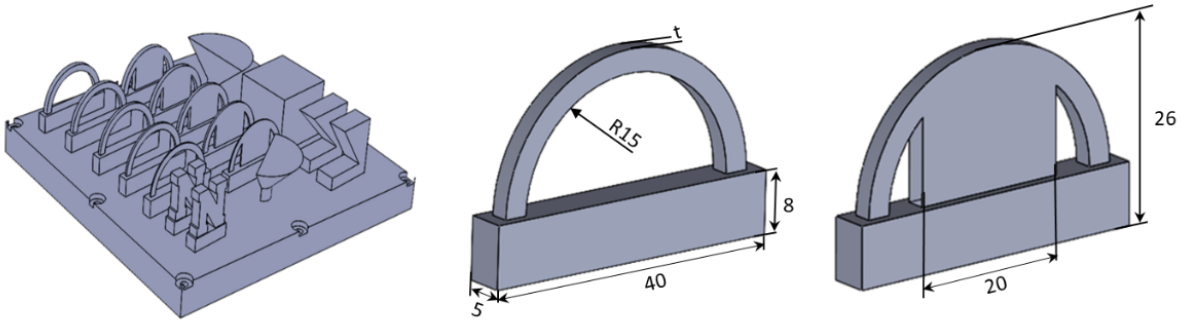

Figure 15: The layout of the build plate, and arch-shaped geometries (with and without supports) with varying gauge thicknesses, t = 0.5, 1.0, 1.5, 2.0, and 2.5 mm.

The arches are labeled per their gauge thickness, as follows: the arch with thickness t = 0.5 mm is labeled as A05; t = 1.0 mm as A10; t = 1.5 mm as A15; and so on. The arches with supports are labeled as SA05, SA10, and so on. Each arch consists of 650 layers at a layer height of 40 µm. The clearance between the recoater and powder bed is also 40 µm. The arches A05 and A10 had recoater crashes at layer 556 and 548, respectively, corresponding to the build height of 22 mm; arches A20 and A25 crashed at a build height of 23 mm corresponding to layer 574. Arch A15 did not experience a recoater crash as it was protected by neighboring arches.

To explain further, the superelevation of the arches on either side of A15 (A10 and A20) lifted the recoater blade and created sufficient clearance to prevent contact with the part. Representative thermal camera frames corresponding to the layers where the unsupported arches underwent recoater crashes are shown in Figure 16.

These recoater crash events are evident from the infrared thermal image. After the recoater crash event of arch A10 at layer 548, higher thermal intensity is recorded in its location compared to the rest of the arches at that same layer. To explain further, following the breakage of the arch A10 due to the recoater crash, the laser scans an area of the powder bed without a solid part underneath. Since compared to a solid part, powder is a poor conductor of heat, the temperature of the powder bed increases. The same heat retention phenomena are also evident with the recoater crashes of the arches A05, A20, and A25 corresponding to layers 556 and 574. Indeed, the debris from arch A10 is observed at layer 574 in the thermal image, nearly 25 layers after the recoater crash. Ten arches (five arches with supports and five arches without supports) were simulated (one at a time). For brevity, the results of four representative arches A10, A20, A25, and SA25 are reported. The boundary conditions, material properties, and simulation parameters are reported in Table 1.

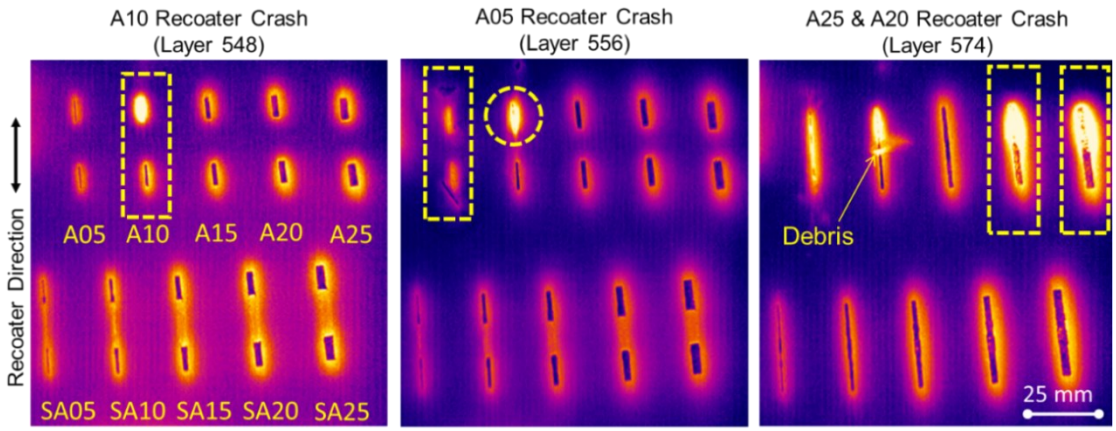

Figure 16: IR camera images of recoater crash incidents at layers 548, 556, and 574 corresponding to arches A10, A05, and A25 & A20. Note that the relative intensity of the failed arches is higher

compared to the other arches due to heat retention following the recoater crash The debris of the crashed arch A10 is still evident in the subsequent layers. Image from Yavari *et al.* [56].

4.2 Prediction of Thermal History

In Figure 17, the surface temperature at the end of a layer is predicted using the graph theory, and results from the coupled thermomechanical FE models are overlaid on the experimental data. It is observed that both the graph theory thermal model and coupled thermomechanical FE model track the experimental thermal observation up to the point of the recoater crash. The thermal prediction results are summarized in Table 7. The graph theory approach predicts the temperature distribution within MAPE 5%, and 20 °C RMSE in less than 4 minutes. In comparison the FE model requires 30 minutes to reach the same level of error.

In Figure 17(b)-(c), the mismatch in the observed temperature, and FE and graph theory predictions in the vicinity of layer 200 for the arches without supports is likely due to the super layer assumption. As explained in Sec. 2.2, the FE and graph theory approach make the super layer assumption to simplify computation, in this work the super layer thickness (Table 1) was fixed at 0.5 mm (12.5 layers). As a result of the super layer assumption, when the cross-section of the part changes rather rapidly around the layer 200 mark (beginning of arch-section), both the FE and graph theory model are reticent in capturing this change. This deficiency can be overcome by reducing the super layer thickness, albeit at the cost of computation time.

A qualitative comparison of the thermal prediction of two types of arches – arch without supports (A25), and arch with supports (SA25) – at three different build heights is shown in Figure 18. The thermal fields of the FE, graph theory (Thermal), and Netfabb models show that the arch without supports (A25) accumulates heat as it builds up. At one point, the heat retention caused enough deformation in the build direction to interfere with the recoater which ultimately caused

the recoater crash. Meanwhile, for the arch with supports (SA25), the supports created a conductive path between the thin legs and the base that prevented heat accumulation. As a result, heat-induced deformation is relatively low and no subsequent recoater crash occurred.

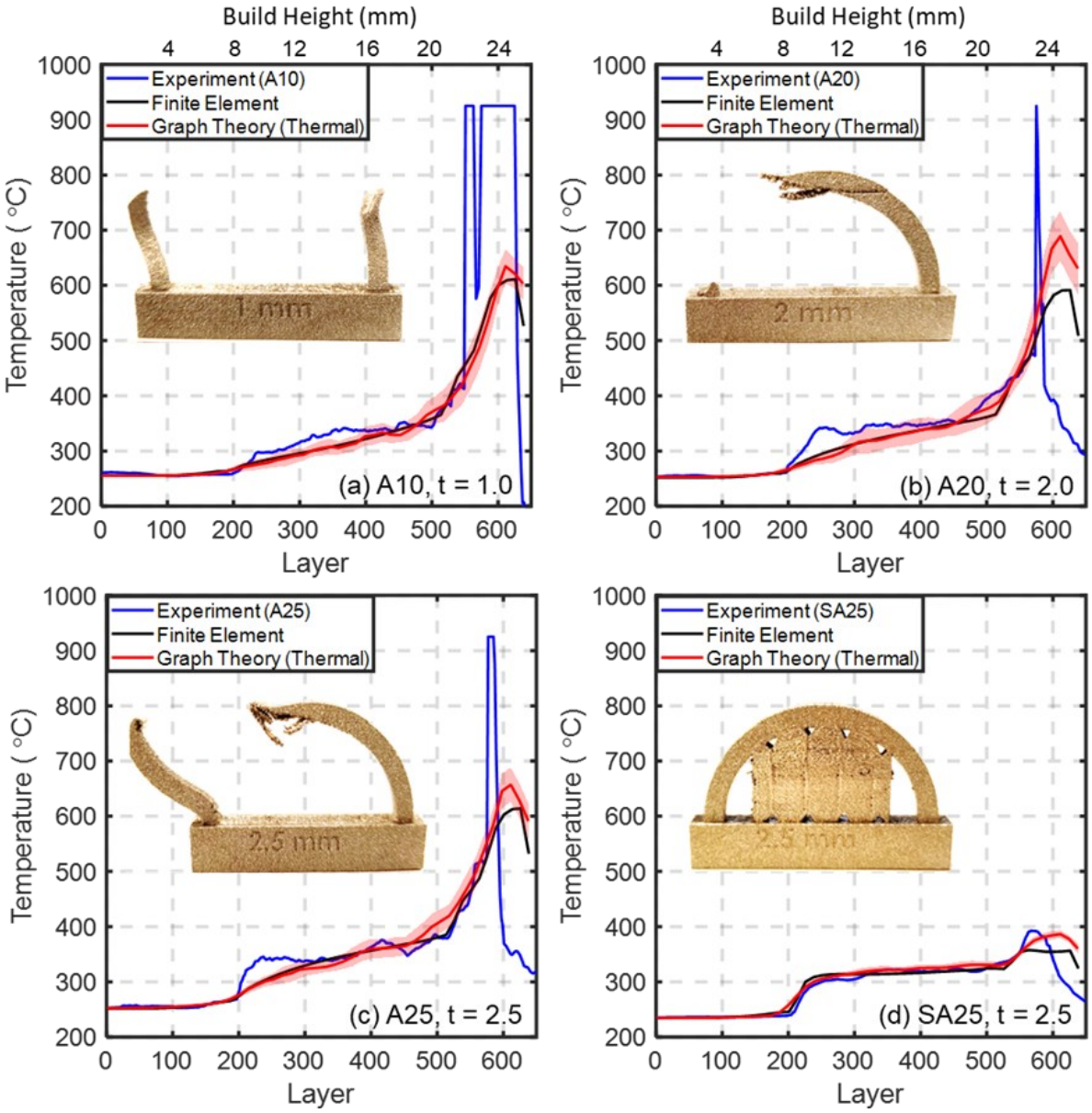

Figure 17: The surface temperature observed during experiments (blue line) overlaid on the coupled thermomechanical FE model (black), and graph theory (red) thermal history predictions for four representative arches (a) A10, (b) A20, (c) A25, and (d) SA25.

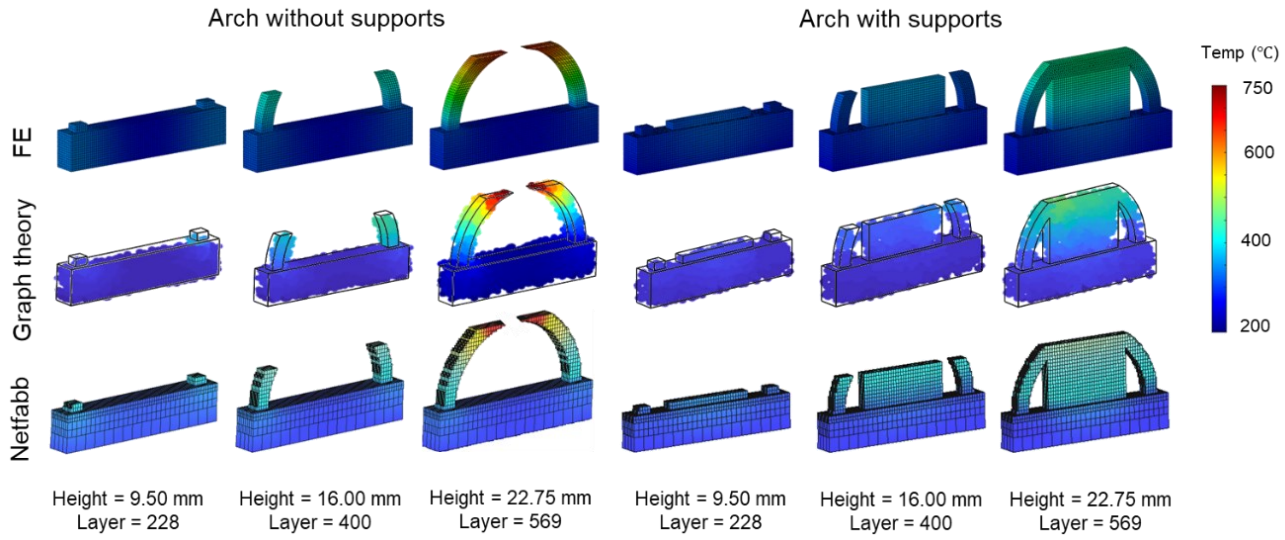

Figure 18: Qualitative comparison of the thermal history predictions for arches 2.5 mm with (SA25) and without (A25) supports at the completion of three different build heights from coupled thermomechanical FE model, graph theory, and Netfabb.

Table 7: Coupled thermomechanical FE and graph theory thermal model performance for the estimation of thermal history in terms of MAPE, RMSE, and computation, with respect to experimental data.

Part	Number of Nodes		MAPE before the first crash (Layer 548) (%)		RMSE before the first crash (°C)		Computation Time (s)	
	FE	Graph theory	FE	Graph theory	FE	Graph theory	FE	Graph theory
A10 (Figure 17(a))	17,576	1,920	4.40	3.66	19.85	15.40	1523	193
A20 (Figure 17(b))	20,932	2,155	5.80	3.98	29.05	20.12	1601	214
A25 (Figure 17(c))	23,611	2,260	4.19	3.57	26.63	18.32	1683	224
SA25 (Figure 17(d))	26,554	2,635	2.13	2.03	12.99	8.82	1716	273

4.3 Prediction of Recoater Crash

Deformation predictions from the coupled thermomechanical FE, graph theory, and Netfabb models are shown in Figure 19 and reported in Table 8 and Table 9. The qualitative comparison of deformation predictions from the coupled thermomechanical FE, graph theory, and Netfabb approaches is shown in Figure 20. As is evident, the arches without supports (A10, A20, and A25 in Figure 19(a), Figure 19(b), and Figure 19(c)) deform considerably. When the part reaches nearly 23 mm in height, the deformation exceeds the clearance of 40 μm between the recoater and powder bed, increasing the likelihood of a recoater crash. Meanwhile, the arch with supports, SA25 shows the deformation in the vertical build direction remains below 40 μm as the supports create a conductive path to prevent heat retention. Hence, a recoater crash is unlikely to occur for SA25.

In Table 8, the layer at which a recoater crash is likely to occur is predicted using graph theory, and the results are compared with those from coupled thermomechanical FE and Netfabb. The graph theory approach correctly predicts the moment of the recoater crash for all the unsupported arches, as well as correctly anticipates that a recoater crash is unlikely to occur for the supported arches. The graph theory approach predicted that a recoater crash would occur about 12 layers before the recoater crash is observed in the experiment in the unsupported arches except for the case of the arch A10. Similar results are reported by both the FE and Netfabb models. Moreover, the computation time of the graph theory approach ranges from 3 to 4 minutes, similar to Netfabb. In comparison the FE approach requires over 25 minutes. The graph theory approach predicts deformation within 4 μm of the FE predictions (ground truth).

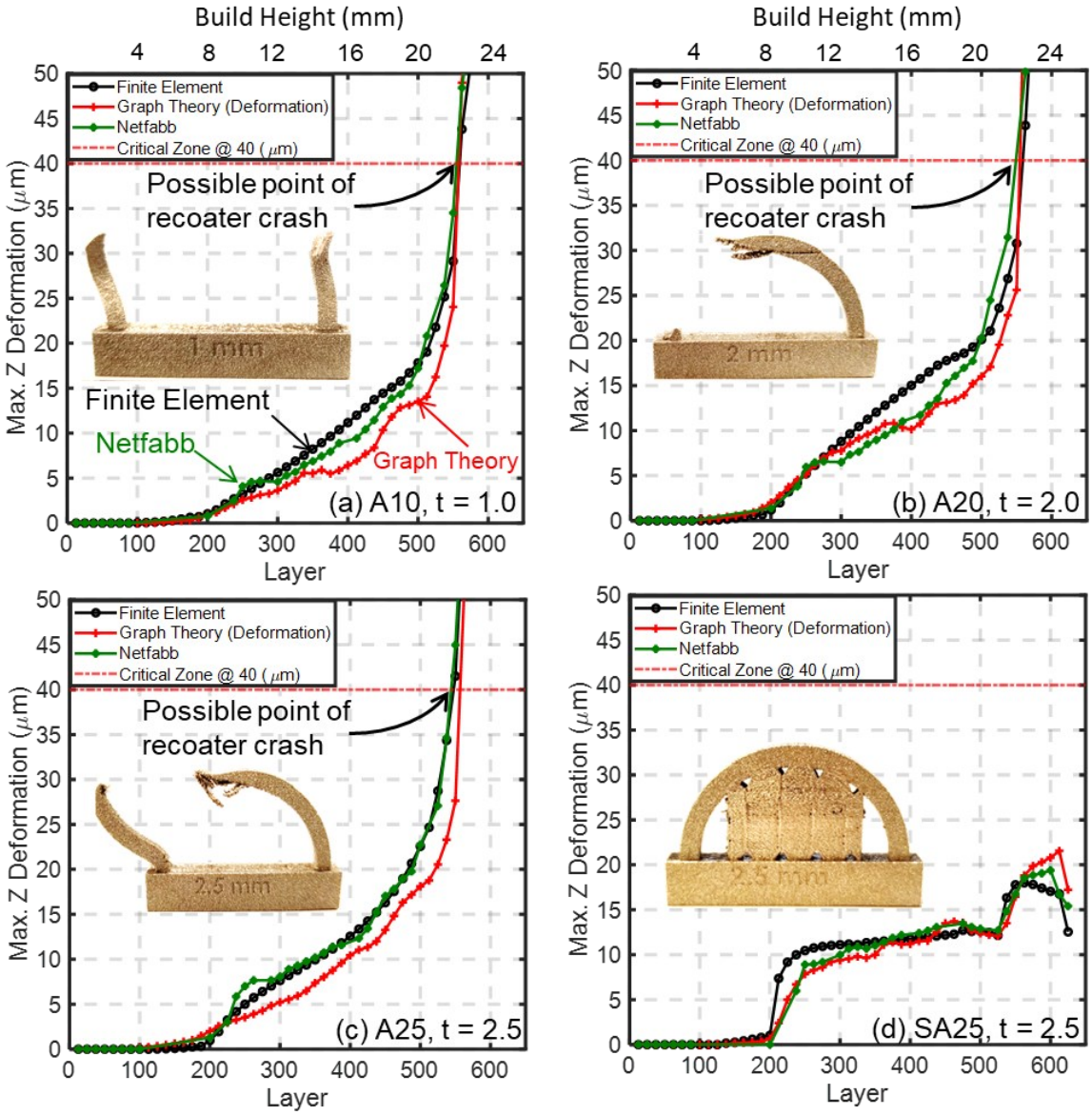

Figure 19: Deformation predictions of each layer using coupled thermomechanical FE (black), graph theory-based (red), and Netfabb (green) models corresponding to the arches (a) A10, (b) A20, (c) A25, and (d) SA25. The recoater crash occurs when deformation exceeds the layer height of 40 µm (red dotted).

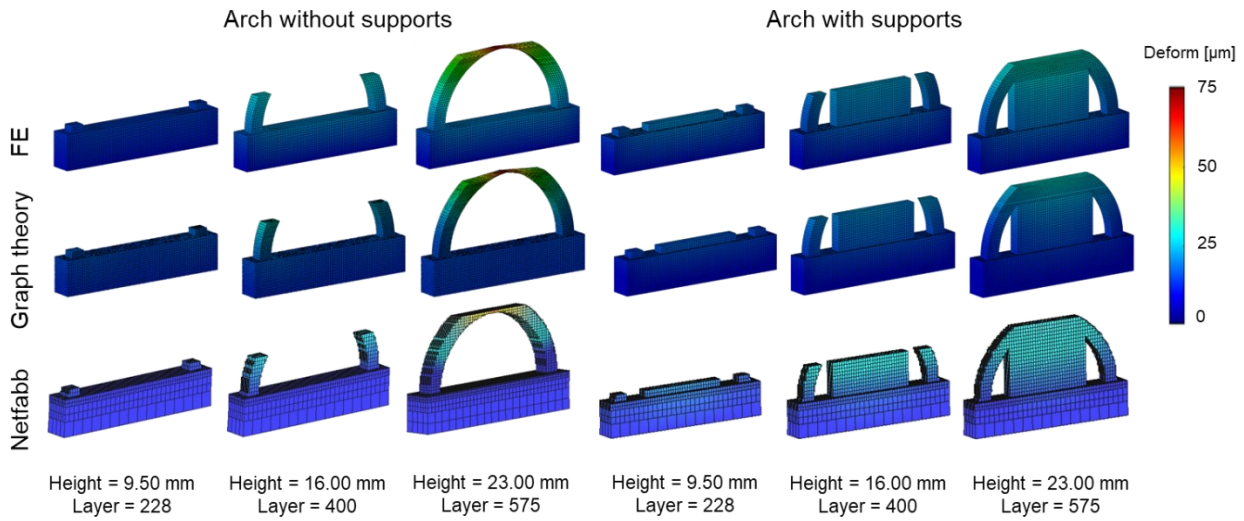

Figure 20: Qualitative comparison of the deformation predictions at three different build heights using coupled thermomechanical FE model, graph theory (Deformation), and Netfabb models of the arch without supports A25 and arch with supports SA25.

Table 8: Summary of experimental recoater crash, and the recoater crash predictions obtained from coupled thermomechanical FE, graph theory (Deformation), and Netfabb approaches, respectively. The number in the parentheses is the computation time in seconds.

Part	Layer at which recoater crash was observed in the experiment	Layer of recoater crash prediction		
		Coupled thermomechanical FE	Graph theory (Deformation)	Netfabb
A05	556	Crash predicted at Layer 538 (1512 seconds computation time)	550 (189)	550 (207)
A10	548	562 (1523)	562 (193)	560 (229)
A15	No crash	562 (1536)	562 (211)	550 (239)
A20	574	562 (1601)	562 (214)	560 (246)
A25	574	550 (1683)	562 (224)	550 (252)
SA25, and all other supported arches	No crash	No crash (1716)	No crash (273)	No crash (351)

Table 9: Summary of Node density, Node count, Mean Percentage Error (MAPE), Root Mean Square Error (RMSE), and computation time for the coupled thermomechanical FE model, graph theory (Deformation), and Netfabb simulations.

Part	Variables	Coupled thermomechanical FE model	Graph theory	Netfabb
A05	Node count	19930	1795	16668
	MAPE (%)	Ground truth	13.79	12.61
	RMSE (μm)	Ground truth	2.54	3.34
	Computation time (s)	1512	189	207
A10	Node count	21588	1920	24370
	MAPE (%)	Ground truth	18.8	9.80
	RMSE (μm)	Ground truth	2.90	2.30
	Computation time (s)	1523	193	229
A15	Node count	23348	2035	26764
	MAPE (%)	Ground truth	18.28	10.29
	RMSE (μm)	Ground truth	2.78	3.77
	Computation time (s)	1536	211	239
A20	Node count	25123	2155	30686
	MAPE (%)	Ground truth	13.00	10.80
	RMSE (μm)	Ground truth	2.60	2.20
	Computation time (s)	1601	214	246
A25	Node count	26678	2260	24896
	MAPE (%)	Ground truth	15.40	13.00
	RMSE (μm)	Ground truth	3.90	3.20
	Computation time (s)	1683	224	252
SA25	Node count	26964	2635	40323
	MAPE (%)	Ground truth	8.40	5.27
	RMSE (μm)	Ground truth	1.60	1.09
	Computation time (s)	1716	273	351

5 Conclusions and Future Work

This work presented a novel graph theory-based approach for thermomechanical modeling in the laser powder bed fusion (LPBF) process. The approach was applied to predict a commonly occurring type of thermal-induced deformation failure in LPBF called recoater crash. The advantage of this approach is its computational efficiency when compared to a coupled thermomechanical FE model. This approach enables the user to rapidly identify part design and processing conditions for avoiding recoater crashes before the part is printed. This work provides an opportunity to evolve from cumbersome and expensive empirical testing to a physics-based strategy for process optimization in LPBF, thus reducing the time-to-market for LPBF parts.

Specific contributions of this work are as follows:

1. The approach was verified with two LPBF test parts. The deformation in the vertical direction was predicted using the graph theory approach and the predictions were compared with the coupled thermomechanical FE analysis which was considered as the ground truth. It was found that the deformation predictions obtained from the graph theory approach closely agreed with the coupled thermomechanical FE solutions. The calculated errors were less than 10% (MAPE), and 10 μm (RMSE). The key result is that the deformation predictions from the graph theory approach converge about 5 times faster than the coupled thermomechanical FE approach.
2. Experimental validation was carried out by building arch-shaped parts. Two types of arches were built, namely, arches with supports and arches without supports. The approach correctly predicted the likelihood of recoater crashes in arches without supports. The results agreed with both coupled thermomechanical FE modeling and commercial software (Autodesk Netfabb). The Netfabb simulation environment is a decoupled

thermo-mechanical solver, developed based on the non-linear FE method for simulation of the AM process. The graph theory approach converged approximately 6 times faster than the coupled thermomechanical FE approach (5 minutes vs 30 minutes) with prediction error less than 4 μm. The computation time of the graph theory approach is similar are to Netfabb.

We will endeavor to answer the following questions in our forthcoming works:

- What is the effect of the thermal history on residual stress? How much would the part distort when removed from the build plate? What is the likelihood of supports failure on account of thermal deformation?
- What is the effect of thermal-induced deformation on the geometric aspects, such as circularity, planarity, straightness, etc.? Subsequently, how should the part design be changed to compensate for thermal deformation.
- What is the effect of thermal history on sub-millimeter flaws, such as hot spots, cracking, and lack-of-fusion?

Lastly, to accommodate fine features and support structures, we are currently establishing an adaptive node generation approach in graph theory, wherein fine features are populated with higher density of nodes (smaller neighborhood radius ε), and larger features are populated with low density nodes.

References Cited

[1] Sames, W. J., List, F., Pannala, S., Dehoff, R. R., and Babu, S. S., 2016, "The metallurgy and processing science of metal additive manufacturing," International Materials Reviews, **61**(5), pp. 315-360. doi: 10.1080/09506608.2015.1116649

[2] Tofail, S. A. M., Koumoulos, E. P., Bandyopadhyay, A., Bose, S., O'Donoghue, L., and Charitidis, C., 2018, "Additive manufacturing: scientific and technological challenges, market uptake and opportunities," Materials Today, **21**(1), pp. 22-37. doi: https://doi.org/10.1016/j.mattod.2017.07.001

[3] Bourell, D. L., 2016, "Perspectives on Additive Manufacturing," Annual Review of Materials Research, **46**(1), pp. 1-18. doi: 10.1146/annurev-matsci-070115-031606

[4] Kellner, T., 2018, "Fired Up: GE Successfully Tested Its Advanced Turboprop Engine With 3D-Printed Parts," GE reports.

[5] DebRoy, T., Wei, H., Zuback, J., Mukherjee, T., Elmer, J., Milewski, J., Beese, A., Wilson-Heid, A., De, A., and Zhang, W., 2018, "Additive manufacturing of metallic components–process, structure and properties," Progress in Materials Science, **92**, pp. 112-224. doi:

[6] Gorelik, M., 2017, "Additive manufacturing in the context of structural integrity," International Journal of Fatigue, **94**, pp. 168-177. doi: https://doi.org/10.1016/j.ijfatigue.2016.07.005

[7] Uriondo, A., Esperon-Miguez, M., and Perinpanayagam, S., 2015, "The present and future of additive manufacturing in the aerospace sector: A review of important aspects," Proceedings of the Institution of Mechanical Engineers, Part G: Journal of Aerospace Engineering, **229**(11), pp. 2132-2147. doi: 10.1177/0954410014568797

[8] Seifi, M., Salem, A., Beuth, J., Harrysson, O., and Lewandowski, J. J., 2016, "Overview of Materials Qualification Needs for Metal Additive Manufacturing," JOM, **68**(3), pp. 747-764. doi: 10.1007/s11837-015-1810-0

[9] Gorelik, M., 2016, "Additive manufacturing and risk mitigation–a regulatory perspective," Proc. FAA-AF Additive Manufacturing Workshop, Dayton, OH, USA. In: DOT/FAA/TC-16/15.

[10] Seifi, M., Gorelik, M., Waller, J., Hrabe, N., Shamsaei, N., Daniewicz, S., and Lewandowski, J. J., 2017, "Progress Towards Metal Additive Manufacturing Standardization to Support Qualification and Certification," JOM, **69**(3), pp. 439-455. doi: 10.1007/s11837-017-2265-2

[11] Thomas-Seale, L. E. J., Kirkman-Brown, J. C., Attallah, M. M., Espino, D. M., and Shepherd, D. E. T., 2018, "The barriers to the progression of additive manufacture: Perspectives from UK industry," International Journal of Production Economics, **198**, pp. 104-118. doi: https://doi.org/10.1016/j.ijpe.2018.02.003

[12] Diegel, O., Nordin, A., and Motte, D., 2019, A Practical Guide to Design for Additive Manufacturing, Springer.

[13] Diegel, O., and Wohlers, T., 2019, "Understanding build failures in Laser Powder Bed Fusion: An overview," Metal AM,Vol 5,Issue: 1,

[14] Bandyopadhyay, A., and Traxel, K. D., 2018, "Invited review article: Metal-additive manufacturing—Modeling strategies for application-optimized designs," Additive Manufacturing, **22**, pp. 758-774. doi: https://doi.org/10.1016/j.addma.2018.06.024

[15] Martin, A. A., Calta, N. P., Khairallah, S. A., Wang, J., Depond, P. J., Fong, A. Y., Thampy, V., Guss, G. M., Kiss, A. M., Stone, K. H., Tassone, C. J., Nelson Weker, J., Toney, M. F., van Buuren, T., and Matthews, M. J., 2019, "Dynamics of pore formation during laser powder bed fusion additive manufacturing," Nature Communications, **10**(1), p. 1987. doi: 10.1038/s41467-019-10009-2

[16] Wei, H. L., Mukherjee, T., Zhang, W., Zuback, J. S., Knapp, G. L., De, A., and DebRoy, T., 2021, "Mechanistic models for additive manufacturing of metallic components," Progress in Materials Science, **116**, p. 100703. doi: https://doi.org/10.1016/j.pmatsci.2020.100703

[17] Hooper, P. A., 2018, "Melt pool temperature and cooling rates in laser powder bed fusion," Additive Manufacturing, **22**, pp. 548-559. doi: https://doi.org/10.1016/j.addma.2018.05.032

[18] Francois, M. M., Sun, A., King, W. E., Henson, N. J., Tourret, D., Bronkhorst, C. A., Carlson, N. N., Newman, C. K., Haut, T., Bakosi, J., Gibbs, J. W., Livescu, V., Vander Wiel, S. A., Clarke, A. J., Schraad, M. W., Blacker, T., Lim, H., Rodgers, T., Owen, S., Abdeljawad, F., Madison, J., Anderson, A. T., Fattebert, J. L., Ferencz, R. M., Hodge, N. E., Khairallah, S. A., and Walton, O., 2017, "Modeling of additive manufacturing processes for metals: Challenges and opportunities," Current Opinion in Solid State and Materials Science, **21**(4), pp. 198-206. doi: https://doi.org/10.1016/j.cossms.2016.12.001

[19] Khairallah, S. A., Anderson, A. T., Rubenchik, A., and King, W. E., 2016, "Laser powder-bed fusion additive manufacturing: Physics of complex melt flow and formation mechanisms of pores, spatter, and denudation zones," Acta Materialia, **108**, pp. 36-45. doi: 10.1016/j.actamat.2016.02.014

[20] King, W., Anderson, A., Ferencz, R., Hodge, N., Kamath, C., and Khairallah, S., 2014, "Overview of modelling and simulation of metal powder-bed fusion process at Lawrence Livermore National Laboratory," Materials Science and Technology, **31**(8), pp. 957-968. doi:

[21] Dovgyy, B., Piglione, A., Hooper, P. A., and Pham, M.-S., 2020, "Comprehensive assessment of the printability of CoNiCrFeMn in Laser Powder Bed Fusion," Materials & Design, **194**, p. 108845. doi: https://doi.org/10.1016/j.matdes.2020.108845

[22] Spears, T. G., and Gold, S. A., 2016, "In-process sensing in selective laser melting (SLM) additive manufacturing," Integrating Materials and Manufacturing Innovation, **5**(1), pp. 16-40. doi: 10.1186/s40192-016-0045-4

[23] Cheng, L., Liang, X., Bai, J., Chen, Q., Lemon, J., and To, A., 2019, "On utilizing topology optimization to design support structure to prevent residual stress induced build failure in laser powder bed metal additive manufacturing," Additive Manufacturing, **27**, pp. 290-304. doi: https://doi.org/10.1016/j.addma.2019.03.001

[24] Williams, R. J., Piglione, A., Rønneberg, T., Jones, C., Pham, M.-S., Davies, C. M., and Hooper, P. A., 2019, "In situ thermography for laser powder bed fusion: Effects of layer temperature on porosity, microstructure and mechanical properties," Additive Manufacturing, **30**, p. 100880. doi: https://doi.org/10.1016/j.addma.2019.100880

[25] Gouge, M., and Michaleris, P., 2018, "Chapter 1 - An Introduction to Additive Manufacturing Processes and Their Modeling Challenges," Thermo-Mechanical Modeling of Additive Manufacturing, M. Gouge, and P. Michaleris, eds., Butterworth-Heinemann, pp. 3-18.

[26] Gouge, M., and Michaleris, P., 2018, "Thermo-Mechanical Modeling of Additive Manufacturing," Elsevier, Cambridge, MA. doi:

[27] Gouge, M., Denlinger, E., Irwin, J., Li, C., and Michaleris, P., 2019, "Experimental validation of thermo-mechanical part-scale modeling for laser powder bed fusion processes," Additive Manufacturing, **29**, p. 100771. doi: https://doi.org/10.1016/j.addma.2019.06.022

[28] Luo, Z., and Zhao, Y., 2018, "A survey of finite element analysis of temperature and thermal stress fields in powder bed fusion Additive Manufacturing," Additive Manufacturing, **21**, pp. 318-332. doi: 10.1016/j.addma.2018.03.022

[29] DebRoy, T., Wei, H. L., Zuback, J. S., Mukherjee, T., Elmer, J. W., Milewski, J. O., Beese, A. M., Wilson-Heid, A., De, A., and Zhang, W., 2018, "Additive manufacturing of metallic components – Process, structure and properties," Progress in Materials Science, **92**, pp. 112-224. doi: https://doi.org/10.1016/j.pmatsci.2017.10.001

[30] Schoinochoritis, B., Chantzis, D., and Salonitis, K., 2017, "Simulation of metallic powder bed additive manufacturing processes with the finite element method: A critical review," Proceedings of the Institution of Mechanical Engineers, Part B: Journal of Engineering Manufacture, **231**(1), pp. 96-117. doi: 10.1177/0954405414567522

[31] Nickel, A. H., Barnett, D. M., and Prinz, F. B., 2001, "Thermal stresses and deposition patterns in layered manufacturing," Materials Science and Engineering: A, **317**(1), pp. 59-64. doi: https://doi.org/10.1016/S0921-5093(01)01179-0

[32] Dai, K., and Shaw, L., 2004, "Thermal and mechanical finite element modeling of laser forming from metal and ceramic powders," Acta Materialia, **52**(1), pp. 69-80. doi: https://doi.org/10.1016/j.actamat.2003.08.028

[33] Song, X., Xie, M., Hofmann, F., Illston, T., Connolley, T., Reinhard, C., Atwood, R. C., Connor, L., Drakopoulos, M., Frampton, L., and Korsunsky, A. M., 2015, "Residual stresses and microstructure in Powder Bed Direct Laser Deposition (PB DLD) samples," International Journal of Material Forming, **8**(2), pp. 245-254. doi: 10.1007/s12289-014-1163-1

[34] Denlinger, E. R., Irwin, J., and Michaleris, P., 2014, "Thermomechanical Modeling of Additive Manufacturing Large Parts," Journal of Manufacturing Science and Engineering, **136**(6) doi: 10.1115/1.4028669

[35] Lindgren, L.-E., Lundbäck, A., Fisk, M., Pederson, R., and Andersson, J., 2016, "Simulation of additive manufacturing using coupled constitutive and microstructure models," Additive Manufacturing, **12**, pp. 144-158. doi: https://doi.org/10.1016/j.addma.2016.05.005

[36] Matsumoto, M., Shiomi, M., Osakada, K., and Abe, F., 2002, "Finite element analysis of single layer forming on metallic powder bed in rapid prototyping by selective laser processing," International Journal of Machine Tools and Manufacture, **42**(1), pp. 61-67. doi: https://doi.org/10.1016/S0890-6955(01)00093-1

[37] Dunbar, A. J., Denlinger, E. R., Gouge, M. F., and Michaleris, P., 2016, "Experimental validation of finite element modeling for laser powder bed fusion deformation," Additive Manufacturing, **12**, pp. 108-120. doi: https://doi.org/10.1016/j.addma.2016.08.003

[38] Ganeriwala, R., and Zohdi, T. I., 2016, "A coupled discrete element-finite difference model of selective laser sintering," Granular Matter, **18**(2), p. 21. doi:

[39] Yang, Y., Allen, M., London, T., and Oancea, V., 2019, "Residual Strain Predictions for a Powder Bed Fusion Inconel 625 Single Cantilever Part," Integrating Materials and Manufacturing Innovation, **8**(3), pp. 294-304. doi: 10.1007/s40192-019-00144-5

[40] Williams, R. J., Davies, C. M., and Hooper, P. A., 2018, "A pragmatic part scale model for residual stress and distortion prediction in powder bed fusion," Additive Manufacturing, **22**, pp. 416-425. doi: https://doi.org/10.1016/j.addma.2018.05.038

[41] Mukherjee, T., Zhang, W., and DebRoy, T., 2017, "An improved prediction of residual stresses and distortion in additive manufacturing," Computational Materials Science, **126**, pp. 360-372. doi: https://doi.org/10.1016/j.commatsci.2016.10.003

[42] Josupeit, S., Ordia, L., and Schmid, H.-J., 2016, "Modelling of temperatures and heat flow within laser sintered part cakes," Additive Manufacturing, **12**, pp. 189-196. doi: https://doi.org/10.1016/j.addma.2016.06.002

[43] Hodge, N. E., Ferencz, R. M., and Vignes, R. M., 2016, "Experimental comparison of residual stresses for a thermomechanical model for the simulation of selective laser melting," Additive Manufacturing, **12**, pp. 159-168. doi: https://doi.org/10.1016/j.addma.2016.05.011

[44] Afazov, S., Denmark, W. A. D., Lazaro Toralles, B., Holloway, A., and Yaghi, A., 2017, "Distortion prediction and compensation in selective laser melting," Additive Manufacturing, **17**, pp. 15-22. doi: https://doi.org/10.1016/j.addma.2017.07.005

[45] Marques, B. M., Andrade, C. M., Neto, D. M., Oliveira, M. C., Alves, J. L., and Menezes, L. F., 2020, "Numerical Analysis of Residual Stresses in Parts Produced by Selective Laser Melting Process," Procedia Manufacturing, **47**, pp. 1170-1177. doi: https://doi.org/10.1016/j.promfg.2020.04.167

[46] Desmaison, O., Pires, P.-A., Levesque, G., Peralta, A., Sundarraj, S., Makinde, A., Jagdale, V., and Megahed, M., 2017, "Influence of Computational Grid and Deposit Volume on Residual Stress and Distortion Prediction Accuracy for Additive Manufacturing Modeling," Proc. Proceedings of the 4th World Congress on Integrated Computational Materials Engineering (ICME 2017), pp. 365-374.

[47] Peter, N., Pitts, Z., Thompson, S., and Saharan, A., 2020, "Benchmarking build simulation software for laser powder bed fusion of metals," Additive Manufacturing, **36**, p. 101531. doi: https://doi.org/10.1016/j.addma.2020.101531

[48] Baiges, J., Chiumenti, M., Moreira, C. A., Cervera, M., and Codina, R., 2021, "An adaptive Finite Element strategy for the numerical simulation of additive manufacturing processes," Additive Manufacturing, **37**, p. 101650. doi: https://doi.org/10.1016/j.addma.2020.101650

[49] Peng, H., Ghasri-Khouzani, M., Gong, S., Attardo, R., Ostiguy, P., Gatrell, B. A., Budzinski, J., Tomonto, C., Neidig, J., Shankar, M. R., Billo, R., Go, D. B., and Hoelzle, D., 2018, "Fast prediction of thermal distortion in metal powder bed fusion additive manufacturing: Part 1, a thermal circuit network model," Additive Manufacturing, **22**, pp. 852-868. doi: https://doi.org/10.1016/j.addma.2018.05.023

[50] Chowdhury, S., and Anand, S., 2016, "Artificial Neural Network Based Geometric Compensation for Thermal Deformation in Additive Manufacturing Processes," Proc. ASME 2016 11th International Manufacturing Science and Engineering ConferenceV003T08A006.

[51] Francis, J., and Bian, L., 2019, "Deep Learning for Distortion Prediction in Laser-Based Additive Manufacturing using Big Data," Manufacturing Letters, **20**, pp. 10-14. doi: https://doi.org/10.1016/j.mfglet.2019.02.001

[52] Zhu, Q., Liu, Z., and Yan, J., 2021, "Machine learning for metal additive manufacturing: predicting temperature and melt pool fluid dynamics using physics-informed neural networks," Computational Mechanics, **67**(2), pp. 619-635. doi: 10.1007/s00466-020-01952-9

[53] Cole, K. D., Yavari, M. R., and Rao, P. K., 2020, "Computational heat transfer with spectral graph theory: Quantitative verification," International Journal of Thermal Sciences, **153**, p. 106383. doi: https://doi.org/10.1016/j.ijthermalsci.2020.106383

[54] Reza Yavari, M., Williams, R. J., Cole, K. D., Hooper, P. A., and Rao, P., 2020, "Thermal Modeling in Metal Additive Manufacturing Using Graph Theory: Experimental Validation With Laser Powder Bed Fusion Using In Situ Infrared Thermography Data," Journal of Manufacturing Science and Engineering, **142**(12) doi: 10.1115/1.4047619

[55] Yavari, M. R., Cole, K. D., and Rao, P., 2019, "Thermal Modeling in Metal Additive Manufacturing Using Graph Theory," Journal of Manufacturing Science and Engineering, **141**(7) doi: 10.1115/1.4043648

[56] Yavari, R., Smoqi, Z., Riensche, A., Bevans, B., Kobir, H., Mendoza, H., Song, H., Cole, K., and Rao, P., 2021, "Part-scale thermal simulation of laser powder bed fusion using graph theory: Effect of thermal history on porosity, microstructure evolution, and recoater crash," Materials & Design, **204**, p. 109685. doi: https://doi.org/10.1016/j.matdes.2021.109685

[57] Yavari, R., Williams, R., Riensche, A., Hooper, P. A., Cole, K. D., Jacquemetton, L., Halliday, H., and Rao, P. K., 2021, "Thermal modeling in metal additive manufacturing using graph theory – Application to laser powder bed fusion of a large volume impeller," Additive Manufacturing, **41**, p. 101956. doi: https://doi.org/10.1016/j.addma.2021.101956

[58] Escolano, F., Hancock, E. R., and Lozano, M. A., 2012, "Heat diffusion: Thermodynamic depth complexity of networks," Physical Review E, **85**(3), p. 036206. doi: 10.1103/PhysRevE.85.036206

[59] Saito, N., 2013, "Tutorial: Laplacian Eigenfunctions - Foundations and Applications," University of California, Davis, Graduate University for Advanced Studies, National Institute of Fusion Science, Japan. doi:

[60] Xiao, B., Hancock, E. R., and Wilson, R. C., 2009, "Graph characteristics from the heat kernel trace," Pattern Recognition, **42**(11), pp. 2589-2606. doi: https://doi.org/10.1016/j.patcog.2008.12.029

[61] Zhang, F., and Hancock, E. R., 2008, "Graph spectral image smoothing using the heat kernel," Pattern Recognition, **41**(11), pp. 3328-3342. doi: https://doi.org/10.1016/j.patcog.2008.05.007

[62] Liang, X., Hayduke, D., and To, A. C., 2021, "An enhanced layer lumping method for accelerating simulation of metal components produced by laser powder bed fusion," Additive Manufacturing, **39**, p. 101881. doi: https://doi.org/10.1016/j.addma.2021.101881

[63] Peng, H., Go, D. B., Billo, R., Gong, S., Shankar, M. R., Gatrell, B. A., Budzinski, J., Ostiguy, P., Attardo, R., and Tomonto, C., 2016, "Part-scale model for fast prediction of thermal distortion in DMLS additive manufacturing; Part 2: a quasi-static thermo-mechanical model," Proc. Solid Freeform Fabrication Symposium, pp. 382-397.

[64] Peng, H., Ghasri-Khouzani, M., Gong, S., Attardo, R., Ostiguy, P., Rogge, R. B., Gatrell, B. A., Budzinski, J., Tomonto, C., Neidig, J., Shankar, M. R., Billo, R., Go, D. B., and Hoelzle, D., 2018, "Fast prediction of thermal distortion in metal powder bed fusion additive manufacturing: Part 2, a quasi-static thermo-mechanical model," Additive Manufacturing, **22**, pp. 869-882. doi: https://doi.org/10.1016/j.addma.2018.05.001

[65] Thabet, S., and Hullo, J.-F., 2020, "Laplacian Eigenmaps with variational circuits: a quantum embedding of graph data," arXiv preprint arXiv:2011.05128 doi:

[66] Cole, K. D., Riensche, A., and Rao, P. K., 2022, "Discrete Green's functions and spectral graph theory for computationally efficient thermal modeling," International Journal of Heat and Mass Transfer, **183**, p. 122112. doi: https://doi.org/10.1016/j.ijheatmasstransfer.2021.122112

[67] Chen, F., and Yan, W., 2020, "High-fidelity modelling of thermal stress for additive manufacturing by linking thermal-fluid and mechanical models," Materials & Design, **196**, p. 109185. doi: https://doi.org/10.1016/j.matdes.2020.109185

[68] Stavropoulos, P., Foteinopoulos, P., Papacharalampopoulos, A., and Tsoukantas, G., 2019, "Warping in SLM additive manufacturing processes: estimation through thermo-mechanical analysis," The International Journal of Advanced Manufacturing Technology, **104**(1), pp. 1571-1580. doi: 10.1007/s00170-019-04105-2

[69] Mirkoohi, E., Dobbs, J. R., and Liang, S. Y., 2020, "Analytical mechanics modeling of in-process thermal stress distribution in metal additive manufacturing," Journal of Manufacturing Processes, **58**, pp. 41-54. doi: https://doi.org/10.1016/j.jmapro.2020.08.009

[70] Bugatti, M., and Semeraro, Q., 2018, "Limitations of the inherent strain method in simulating powder bed fusion processes," Additive Manufacturing, **23**, pp. 329-346. doi: https://doi.org/10.1016/j.addma.2018.05.041

[71] Cheng, B., and Chou, Y. K., 2015, "Thermal Simulations for Cooling Rate Mapping in Electron Beam Additive Manufacturing," Proc. ASME 2015 International Mechanical Engineering Congress and ExpositionV02AT02A013.

[72] Manshoori Yeganeh, A., Movahhedy, M. R., and Khodaygan, S., 2019, "An efficient scanning algorithm for improving accuracy based on minimising part warping in selected laser sintering process," Virtual and Physical Prototyping, **14**(1), pp. 59-78. doi: 10.1080/17452759.2018.1511738

[73] Prabhakar, P., Sames, W. J., Dehoff, R., and Babu, S. S., 2015, "Computational modeling of residual stress formation during the electron beam melting process for Inconel 718," Additive Manufacturing, **7**, pp. 83-91. doi:

[74] 2022, "Langley Alloys, Alloy 718 (UNS N07718) Materials Datasheet https://www.langleyalloys.com/products/alloy-718/."

Conflict of Interest Statement

On behalf of all authors, the corresponding author states that there is no conflict of interest.

Acknowledgements

Prahalada Rao acknowledges funding from the Department of Energy (DOE), Office of Science, under Grant number DE-SC0021136, and the National Science Foundation (NSF) [Grant numbers CMMI-1719388, OIA-1929172 CMMI-1920245, CMMI-1739696, CMMI-1752069, PFI-TT 2044710, ECCS 2020246] for funding his research program. This work espousing the concept of graph theory thermal modeling for predicting deformation was funded through the NSF Grant OIA 1929172 (Program Officer: Jose Colom). The experiments at Edison Welding Institute used in this work were made possible by the foregoing OIA grant. This grant also supported the graduate work of Dr. Reza Yavari, Mr. Alex Riensche, Mr. Ben Bevans, and Mr. M. H. Kobir. The concept of graph theory thermal modeling was first proposed in CMMI-1752069 (Program Officer: Kevin Chou). The NSF Intern supplement to the foregoing NSF grant (Program officer: Prakash Balan) allowed Dr. Yavari to conduct experiments on the Open Architecture LPBF platform at Edison Welding Institute. This work takes the first step towards commercialization of the graph theory thermal modeling approach through the NSF grant PFI-TT 2044710 (Program Officer: Samir Iqbal), which is currently supporting the graduate work of Mr. Alex Riensche and Mr. Leandro Castro. The DoE grant DE-SC0021136 (Program Officer: Timothy Fitzsimmons) also supported the doctoral graduate work of Mr. Alex Riensche. and Mr. Ben Bevans. Kevin Cole acknowledges funding from DE-SC0021136 and PFI-TT 2044710.